Interpretation®

Independent Component Analysis for reservoir geomorphology and unsupervised seismic facies classification in the Taranaki Basin, New Zealand.

Journal:	*Interpretation*
Manuscript ID	Draft
Manuscript Type:	2018-04 Machine learning in seismic data analysis
Date Submitted by the Author:	n/a
Complete List of Authors:	Lubo-Robles, David; University of Oklahoma, School of Geology and Geophysics Marfurt, Kurt; University of Oklahoma, College of Earth and Energy;
Keywords:	seismic attributes, Seismic geomorphology, algorithm, interpretation, deepwater
Subject Areas:	Interpretation concepts, algorithms, methods, and tools, Amplitudes, attributes, and subsurface properties

Independent Component Analysis for reservoir geomorphology and unsupervised seismic facies classification in the Taranaki Basin, New Zealand.

David Lubo-Robles [1], and Kurt J. Marfurt [1],

1 The University of Oklahoma, School of Geology and Geophysics

email: davidlubo@ou.edu

email: kmarfurt@ou.edu

ABSTRACT

During the past two decades, the number of volumetric seismic attributes have increased to the point in which interpreters are overwhelmed and cannot analyze all the information available. Principal Component Analysis (PCA) is one of the best-known multivariate analysis technique, and decomposes the input data into lower statistics, mathematically uncorrelated components. Unfortunately, while these components mathematically represent the information in the multiple input data volumes using a smaller number of volumes, they often mix rather than separate geologic features of interest. To address this issue, we implement and evaluate a relatively new unsupervised multi-attribute technique called Independent Component Analysis (ICA), which based on higher order statistics, separates multivariate data into independent subcomponents. We evaluate our algorithm to study the internal architecture of turbiditic channel complexes present in the Moki A sands Formation, Taranaki Basin, New Zealand. We input twelve spectral magnitude components ranging from 25 to 80 Hz into the ICA algorithm and plot three of the resulting independent components against an RGB color scheme to generate a single volume in which different colors correspond to different seismic facies. The results obtained using ICA proved to be superior to the obtained using PCA. Specifically, using ICA we obtain independent components that have better resolution and better separation between geologic features and noise compared to uncorrelated components obtained using PCA. Moreover, with ICA, we are able to geologically analyze the different seismic facies and relate them to sand-prone and mud-prone seismic facies associated with axial and off-axis deposition and cut-and-fill architectures.

INTRODUCTION

In addition to picking horizons, traditional interpretation includes the identification of geological features of interest such as faults, collapse features, channel complexes, salt domes, and mass transport deposits in 3D seismic amplitude volumes. Volumetric seismic attributes such as coherence, curvature, gray-level co-occurrence matrix (GLCM) texture attributes and spectral-decomposition analysis can both accelerate and facilitate this process, enhancing subtle features that may otherwise be overlooked. Depending on the seismic attributes interpreters select, different information is extracted (Infante-Paez and Marfurt, 2017; Infante-Paez, 2018). Therefore, relying solely in a single attribute can lead to an incomplete seismic interpretation in which important geological elements can be overlooked. During the past two decades, the number of volumetric seismic attributes have increased to the point in which interpreters are overwhelmed and cannot analyze all the information available.

Co-rendering using red-green-blue (RGB) or hue-lightness-saturation (HLS) color gamuts provide an efficient means of combining the information content of three volumes. For more than three volumes, one must project the higher dimensional data onto a lower dimensional space. Principal Component Analysis (PCA) (Guo et al., 2009; Chopra and Marfurt, 2014; Zhao et al. 2015; Roden et al., 2015) decomposes multivariate data into linearly uncorrelated components using second order statistics based on the covariance matrix of the data. The first three components are either co-rendered using RGB or interpreted using crossplotting tools. PCA is also widely used as the first iteration for clustering techniques in order to reduce dimensionality of the input data (Zhao et al. 2015; Sinha et al., 2016). The *k*-means algorithm (MacQueen,1967) is a clustering technique in which, after the interpreter decides the number of desired clusters, the distance between the multiattribute data point and the center of the clusters is measured using the Mahalanobis distance. Each data point is associated with the closest cluster

(Zhao et al., 2015). Generative Topographic Maps (GTM) generates a probabilistic representation of the data on a lower dimensional manifold (Roy et al., 2014; Zhao et al., 2015). Perhaps the most widely used clustering technique is Self-Organizing Maps (SOM) in which a lower dimensional manifold is first deformed to represent the data which in turn are projected onto a corresponding latent space (Kohonen 1982; Strecker and Uden, 2002; Coléou et al., 2003; Zhao et al., 2015; Zhao et al., 2016; Marfurt, 2018).

Spectral-decomposition analysis (Sinha et al., 2005; Chopra and Marfurt, 2016) decomposes the seismic volume into a suite of magnitude and phase components at different frequencies that allows the study of geologic features near the limits of seismic resolution, enabling the interpreter to map lateral changes in thickness, lithology, and porosity. A major drawback in spectral-decomposition analysis is that from one 3D amplitude volume one may generate up to 10 to 100 output volumes (Guo et al., 2009), making the selection and visualization of the most important components a cumbersome task. Guo et al. (2009) applied Principal Component Analysis (PCA) to characterize channels draining an unconformity in the Central Basin Platform in Texas, Li et al. (2009) applied Independent Component Analysis (ICA) to a carbonate bank data volume in order to map reef as well as shoaling features. Zanardo Honorio et al., (2014) applied ICA to a fluviodeltaic system in order to map channels.

Inspired by the Zanardo Honorio et al.'s (2014) work, we implemented our own ICA algorithm and applied it to deep water turbidite system in the Taranaki Basin, New Zealand, and compared the results not only to the input data volumes, but also on the more commonly used co-rendered PCA volume.

To illustrate ICA, we consider the popular cocktail-party problem, in which two people are speaking simultaneously in a room where two microphones record the combination of their

voices (Figure 1). The recorded signals $\mathbf{X}=\{\mathbf{X_1},\mathbf{X_2}\}$ are linear mixture of the people's voices $\mathbf{P}=\{\mathbf{P_1},\mathbf{P_2}\}$, which can be written as:

$$\mathbf{X} = \mathbf{AP}, \tag{1}$$

where **A** is an unknown matrix called the mixing matrix, whose parameters are a function of the distances between the microphones and the speakers.

Although the goal is to estimate the people's voices $\mathbf{P_1}$ and $\mathbf{P_2}$, the matrix **A** is unknown, such that $\mathbf{P_1}$ and $\mathbf{P_2}$ cannot be computed directly from **X**. ICA assumes that the components $\mathbf{P_i}$ are statistically independent, allowing the computation of the matrix **A** and its inverse **W** (Hyvärinen and Oja, 2000):

$$\mathbf{P} = \mathbf{WX}. \tag{2}$$

In this study, we begin with an explanation of the differences between Principal Component Analysis and Independent Component Analysis techniques. Using an ICA algorithm developed by Hyvärinen and Oja (2000) for feature extraction and signal separation as a guide, we implement an ICA algorithm that can work on a suite of large, 3D volumetric seismic attributes. The choice of attributes used depends on the geologic target. To study submarine turbidites in the Moki A sands of the Taranaki Basin, New Zealand, we use spectral magnitude components, which are routinely used to image both fluvial and deep-water channel and canyon systems (e.g. Partyka et al., 1999; Marfurt and Kirlin, 2001; Lubo-Robles and Marfurt, 2017). We then analyze these spectral components individually and as input to both PCA and ICA algorithms. We conclude with a discussion of the Independent Component Analysis and its advantages with respect to the well-established Principal Component Analysis. Finally, we add an appendix with mathematical details explaining how the algorithm works.

THEORY

A principal component is a scalar value that represents the projection of a *N*-dimensional sample vector, against a *N*-dimensional eigenvector. This technique is known as Principal Component Analysis (PCA) and, based on Gaussian statistics, decomposes the data into mathematically linearly uncorrelated components. PCA reduces the dimensionality and redundancy of the input multivariate data, but may omit geological features associated with lower reflectivity (Guo et al., 2009). PCA is based on an assumption that the data exhibit Gaussian statistics, allowing the use of second order statistics to decompose the data into orthogonal components sorted based on their variability. Principal components are ranked according to the energy of the input data they represent.

In contrast to PCA, Independent Component Analysis (ICA) is based on higher order statistics, separates a multivariate signal into independent, but not necessarily orthogonal subcomponents, finding a linear representation of non-Gaussian data (Hyvärinen and Oja, 2000). The concept of "independence" provides a means to capture more interesting information from the multivariate data (Zanardo Honorio, et al., 2014). The independent components are not only non-orthogonal but their order is undefined (Figure 2), i.e., the independent components cannot be ranked (Hyvärinen and Oja, 2000; Tibaduiza et al., 2012).

The independent component algorithm that we propose (Figure 3) is based on the FastICA algorithm developed by Hyvärinen and Oja (2000), with modifications in order to implement it using volumetric seismic attributes. In our workflow, we first select the seismic attributes, $\boldsymbol{a}$, based on the geological features of interest and compute their means $\boldsymbol{\mu}$ and standard deviations $\boldsymbol{\sigma}$ in order to apply Z-score normalization. We compute the correlation matrix $\mathbf{C}$ from the scaled parameters and compute its eigenvectors and eigenvalues. To be computationally

efficient, we decimate the data in order to create a representative training data subset $\boldsymbol{a_{tr}}$ from which the unmixing matrix **W** is computed.

After the training data are Z-normalized in order to avoid issues related to different units of the seismic attributes, the data are whitened and filtered using Principal Component Analysis (Stanford, 2018) whereby the eigenvalues retained just exceeding 90% are considered to be signal, and the others to be noise.

To initialize the algorithm, we must assume an initial guess for the unmixing matrix **W**. Instead of using a random initial guess, we generate an initial guess based on the eigenvectors and eigenvalues of the correlation matrix **C** in order to guarantee exact repeatability of the process.

Gaussian behavior has maximum entropy. In ICA, the unmixing matrix **W** is estimated by maximizing the non-Gaussian behavior of the multivariate data measured by an approximation of negentropy (Hyvärinen and Oja, 2000). When convergence is reached, the independent components are computed by projecting the Z-normalized and whitened seismic attributes onto the final unmixing matrix, **W**, obtained from the algorithm. For more information on the mathematical details of the procedure, please refer to Appendix A.

GEOLOGICAL BACKGROUND

The Taranaki Basin is a sedimentary basin located along the western side of the North Island, New Zealand (Palmer, 1985) (Figure 4). The eastern Taranaki Graben Complex and the Western Platform are the two main structural elements of the basin (Pilaar and Wakefield, 1984).

The Western Platform, with a width of more than 100 km, is characterized by 2,000 to 5,000 meters of Late Cretaceous-Recent sediments and represents the offshore part of the

Taranaki Basin (Palmer, 1985). The Western Platform was affected by normal block faulting during the Late Cretaceous-Eocene, but during most of the Tertiary it remained relatively stable (Pilaar and Wakefield, 1984). The Taranaki Graben structure is controlled by movement in the basement and faults developed during the Late Cretaceous – Eocene (Palmer, 1985) with its infill characterized by sedimentary and igneous rocks (Pilaar and Wakefield, 1984).

The Taranaki Basin was initially formed by transcurrent rifting during the Late Cretaceous. Throughout this time, transgressive marine and terrestrial sedimentary rocks of the Pakawau Group were deposited (Thrasher, 1992). The Pakawu Group can be subdivided into the Rakopi and the North Cape Formations. An important characteristic of the Rakopi Formation is that it was deposited under fluvial-lacustrine conditions and has good hydrocarbon source potential (Dauzacker et al., 1996).

The Paleocene to Lower Oligocene is characterized by the deposition of the Kapuni Group, a sequence of sandstones, coal and mudstones lithologies, that overlie the Pakawau Group after a period of transgression. Contrary to the Pakawau Group, the Kapuni Group sedimentation is distributed across all the Taranaki Basin and is not confined only to the Cretaceous Grabens (De Bock, 1994).

After the deposition of marine siltstones and mudstones related to the Turi Formation in the Eocene to Early Oligocene, the Tikorangi Limestone, a bioclastic limestone sequence, was deposited widely in the Taranaki Basin during the Oligocene, and according to De Bock (1994) represents a regional seismic marker.

The Miocene deposits are characterized by detrital sedimentation associated with relative sea-level fluctuations and tectonism associated with deposition of sediments in the South

Taranaki Graben during the Early Miocene and reverse faulting in the South Taranaki Graben during the Late Miocene (De Bock, 1994). Deposition started with deep water mudstones and siltstones represented by the Lower Manganui Formation. In the Early to Middle Miocene, deposition of submarine fans occurred associated with a major regression (De Bock, 1994). These submarine fans were deposited on the basin floor or at the base of continental slope (Dauzacker et al., 1996) and are represented by the Mt Messenger and Moki Formations. These sandstone turbidites are diachronous towards the North (Dauzacker et al., 1996).

During the Middle to Late Miocene, the Moki Formation was buried by progradational deposits of the (Upper) Manganui Formation (Dauzacker et al., 1996). The end of the Miocene was characterized by a sea level falling stage, depositing a sequence of prograding strata known as the Giant Foresets Formation. Pliocene to present day sediments are associated with marine deposition (De Bock, 1994).

The Moki Formation is a fine-grained turbidite sequence (Engbers, 2002) and is comprised of sandstones interbedded with siltstone, bathyal claystone and thin limestones (Bussell, 1994). The Moki Formation can be subdivided into the Moki A sands, Moki B shale and the Moki B sands (Bussell, 1994). The Moki B sands form the lower unit in the Moki Formation and consist of turbidite sheet sands with large laterally extension which were deposited on a basin floor (Engbers, 2002). The Moki B shale represents a period of low sedimentation associated to deposition of bathyal claystones (Engbers, 2002) and it tends to thicken to the East and Northeast (Bussell, 1994). The Moki A sands unit was deposited as a base of slope turbidite (Engbers, 2002) and is characterized by major submarine meandering channel complexes (Bussell, 1994) trending NW-SE (Yagci, 2016). According to Bussell (1994), the Moki B sands has few channels while the Moki A sands are incised by sinusoidal channel

complexes, consistent with a progradation of the slope model. The channel complexes present in the Moki A sands unit are the geological feature of interest in this study.

DATASET

The Tui3D seismic survey is located offshore Taranaki Basin on the southwest coast of the North Island, New Zealand (Figure 4) and was acquired by Veritas DGC Australia Pty. Ltd from March 25, 2003 to May 10, 2003 (Veritas DGC, 2003). The Tui3D seismic volume provided by New Zealand Overseas Petroleum Limited (NZOP) has a surface area of 350 km^2 with streamer separation of 150 m and source separation of 75 m and a 12.5 by 12.5 m bin size.

The Tui3D seismic volume data quality is good, but contaminated by acquisition footprint. A phase shift of 180^o was applied to the volume resulting in a zero-phase American polarity. In addition to the seismic volume, we use the Tui SW-2 well to validate our unsupervised seismic facies analysis.

Seismic attributes and analysis interval

Seismic attributes are powerful tools that quantitatively measure properties including continuity, morphology and frequency, facilitating the identification of turbidites and channel complexes in this seismic data volume. Different attributes highlight different features of interest. Combining them using multi-attribute analysis techniques provides a means to better understand the underlying geological processes and to better characterize the reservoir.

Marfurt (2018) summarizes some of the more commonly used multi-attribute data integration tools, including 3D co-rendering, principal component analysis, and self-organizing maps among other. In this paper, we evaluate the relatively new independent component analysis multi-attribute decomposition technique.

In order to apply the independent component algorithm to make a facies analysis and study the geomorphology of the turbiditic channel complexes in the Moki A sands Formation, several seismic attributes are used as input. The choice of these attributes is critical to obtain satisfactory results. Spectral components are sensitive to both impedance and thickness variations and are thus good candidates for turbidite analysis. We hypothesize that applying ICA to spectral magnitude components will reduce the dimensionality of the data, reject noise and extract the most valuable information components, thus accomplishing our goal of highlighting the turbiditic channels in order to study their internal architecture and facies distribution.

Spectral-decomposition analysis is a powerful technique for studying bed-thickness, lateral changes in porosity, and the presence of hydrocarbons (Sinha et al., 2005; Chopra and Marfurt, 2014) and the sequence stratigraphy and the deposition of a particular system (Marfurt and Kirlin, 2001). The method of choice in this study was the Continuous Wavelet Transform (CWT) decomposing the seismic volume into phase and magnitude components at different time-frequency samples, often improving the temporal and vertical resolution and allowing us to interpret geological features at different scales. These frequency components are similar to applying a bandpass filter to the volume and represent its information at a particular frequency (Chopra and Marfurt, 2015; Chopra and Marfurt, 2016).

Besides an appropriate choice of seismic attributes, another critical factor for multi-attribute facies analysis techniques, is the design of the analysis interval. The ideal analysis interval encloses only the target formation thereby avoiding mixing adjacent facies that have little to do with the target turbidite facies and basin floor matrix. Fewer facies results in easier facies discrimination.

In this study, the Moki A sands unit consists of strong continuous reflectors incised by discontinuous reflectors with variable reflectivity (Figure 5). For this reason, picking a consistent horizon through the Moki A sands Formation is a challenging task. Instead, we picked a horizon along the base of the Tikorangi Limestone, characterized by a strong continuous reflector and similar depositional trend as the Moki Formation, to create phantom horizons bracketing the top and bottom of the Moki A sands Formation resulting in an analysis interval of 300 ms. Although the ideal analysis interval should enclose only one target formation, to completely enclose the channel complexes present in the Moki A sands Formation, our analysis interval brackets the Moki A sands Formation, the Moki B shale and part of the Moki B sands and Upper Manganui Formations.

RESULTS

Seismic geomorphology and facies analysis using spectral magnitude components as input in the independent component analysis

In order to interpret the geomorphology and facies of the channel complexes present in the Moki A sands unit, each spectral magnitude component, independent component and principal component volumes are flattened against the top analysis interval horizon (Horizon A) which is equivalent to extracting a suite of phantom horizons parallel to Horizon A (Figure 6).

Spectral magnitude components are often plotted against a RGB color scheme for their interpretation (Li and Lu, 2014; Li et al., 2018). If we plot different combinations of these spectral components along a phantom Horizon A + 196 ms, we note that the combination of 25-35-45 Hz (Figure 7a) is similar to the combination of 40-50-60 Hz (Figure 7b), even though a small meandering channel (blue arrow) tends to be better resolved in the former. In contrast, the combination of 60-70-80 Hz (Figure 7c) is contaminated by strong acquisition footprint (red

rectangle) but delineates thin beds inside the channels (yellow arrows). If we plot the 25-50-75 Hz (Figure 7d) we note that the infill of the channels tends to tune at the low frequencies while their flanks are more coherent at approximately 50 Hz, also some thin beds tune at high frequencies of approximately 75 Hz. Analyzing the same combinations at Horizon A + 248 ms (Figure 8), we still observe that the infill of the channels tends to tune at low frequencies, the flanks, internal thin beds and acquisition footprint tune at higher frequencies.

Besides the redundant data existing in the spectral component analysis, selection of which combination better represents the turbiditic channels in the Moki A sands Formation can be cumbersome because there are many output components to choose from, requiring manually scrolling and analysis of each combination. The internal architecture of the channel complexes is poorly captured at 10, 15 and 20 Hz. For these reasons, in workflow #1 (Figure 9), we analyze the spectral magnitude components ranging from 25 to 80 Hz with intervals of 5 Hz in the ICA algorithm. Based on the retained variability criteria (Stanford, 2018), the algorithm automatically outputs four principal components, from which the independent components are computed, because they represent 94.04% of the variability of the data (Figure 10a).

Workflow #1 reduces the 12D attribute space to a 4D mathematical space, in which the 12D vectors at each voxel are projected against the whitened eigenvectors and the results projected against the unmixing matrix **W**. Therefore, if we project the independent components against a RGB color scheme, voxels that are projected to similar colors can be considered as similar seismic facies.

Principal components are sorted based on the energy represented by their eigenvalues. Thus the first principal component (PC1) is the strongest in these data and represents 63.52% of the variability (Figure 10a). The corresponding eigenspectrum is approximately flat (Figure 10b)

because the spectral components were spectrally balanced during the CWT spectral decomposition. The second principal component (PC2) is orthogonal to PC1 and represents 16.66% of the data (Figure 10a). The spectrum monotonically decreases to the larger frequencies (Figure 10b) however, because of the ambiguity in the sign of eigenvectors, it could also monotonically increase. The third principal component (PC3) represents 8.11% of the variance (Figure 10a), is orthogonal to PC1 and PC2 and its amplitude changes sign between 45 to 50 Hz (Figure 10b). Finally the fourth principal component (PC4) is orthogonal to PC1, PC2 and PC3 and captures only 5.74% of the variability of the input data (Figure 10a). Guo et al. (2009) observed that because the principal components reside in a mathematical space, where the spectral components are represented as orthogonal uncorrelated components, little physical significance can be assigned to these spectra.

In contrast, the order of the independent components is undefined because they have unit variance. All four components represent similar energy (Figure 11a). For this reason, the order is defined subjectively, using the geologic features as a criterion, with the noisiest energy being defined as IC4. Independent component #1 tends to represent lower frequency features, independent component #2 is higher between 35 to 60 Hz and independent component #3 very low and moderate frequencies of the spectral components (Figure 11b). Independent component 4 monotonically changes from lower to higher frequencies. Because the independent components reside in a space where the spectral components are represented as oblique projections in order to find independent signals, we believe that the ICA spectra has a more physical significance that the PCA eigenspectrum.

Comparing the variability of the principal components to the energy of the independent components, we observe that PCA tends to be dominated by principal component #1 (PC1),

while the independent components exhibit almost the same energy, and thus they are equally important.

In Figure 12 compares principal component 1 (PC1) (Figure 12a) to independent component 1 (IC1) (Figure 12b) along Horizon A + 196 ms. Numbering is used to identify the different architectural elements and is not associated with time of deposition of the channel complexes. On both pictures, we observe the confluence of two leveed meandering tributary channels with moderate sinuosity and a tabular shape channel with an architecture similar to a braided channel, the merging of these three late lowstand turbidite channel infill systems form a major turbidite channel towards the Northwest of the study area.

In addition, we note that IC1 presents better footprint suppression (red rectangle) and a smoother; less noisy picture than PC1. Moreover, the large scale channels (green arrows) and small scale features such as oxbow 1, oxbow 2, oxbow 3 (orange arrows) and a small abandoned meandering channel (blue arrow) are better delineated using IC1 (Figure 12b).

Analyzing the IC1 and PC1 at Horizon A + 248 ms (Figure 13), we notice that the result obtained from the ICA (Figure 13b) still provides better resolution, less random noise and better footprint suppression (red rectangle) than PC1 (Figure 13a). Furthermore, while the leveed meandering channels (green arrows) are difficult to delineate in PC1, these are better resolved using IC1. In addition, the tabular shape channel bifurcates into two distributary channels towards the Northwest and it is being better delineated and internally resolved using IC1. The small scale oxbow 3 (orange arrow) is also better resolved by IC1.

When comparing the PC2 and IC2 volumes at Horizon A + 196 ms (Figure 14), we still observe a smoother, less noisy with better footprint suppression image using ICA (Figure 14b).

Moreover, the IC2 better exhibits than PC2 (Figure 14a) the large scale geological features such as the leveed meandering channels and the tabular shape channel (green arrows) and the small scale geological features such as oxbows (orange arrows) and the small abandoned channel (blue arrow).

At Horizon A + 248 ms, IC2 provides a remarkably better result than PC2 (Figure 15). The leveed meandering tributary channels (green arrows) that are difficult to delineate using PC2, are well resolved using IC2 (Figure 15b). In addition, the latter has less footprint (red rectangle) and less random noise than the former and similar to IC1, the small-scale oxbow 3 (orange arrow) has better resolution in IC2 than in PC2 (Figure 15a).

Now, analyzing Figure 16, we observe at Horizon A + 196 ms that the IC3 has still better footprint suppression than PC3 (red rectangle), even though it has more footprint and random noise than IC1 and IC2. The leveed meandering channels, the tabular shape and the subsequent merged main channels (green arrows), together with the small-scale oxbows (orange arrows) are interpretable on both pictures (Figure 16a and Figure 16b). On the other hand, the small abandoned channel that was not completely delineated in PC1 and PC2, is now visible in PC3, while in IC3 itis barely resolved.

At Horizon A + 248 ms (Figure 17), the leveed meandering tributary channel 1 and 2 are still better delineated in IC3 (Figure 17b), but its resolution increases considerably in PC3 (Figure 17a) compared to PC1 and PC2. In addition, the meandering channels 3 and 4 are resolved on both pictures. Moreover, the oxbow 3 (orange arrow) is delineated on both pictures, but it looks better highlighted using PC3.

PC4 at Horizon A + 196 ms (Figure 18a) and at Horizon A + 248 ms (Figure 19a), still exhibits the footprint (red rectangle) and random noise seen in PC1, PC2 and PC3. Also, the geological deep water architectural elements analyzed before are not as well delineated as in the other principal components. In contrast, IC4 at Horizon A + 196 ms (Figure 18b) and at Horizon A + 248 ms (Figure 19b), is contaminated by strong acquisition footprint and random noise. The architectural elements of IC4 are poorly delineated when compared to ICA1, IC2 and IC3. This observation is consistent with the objective of independent component analysis which seeks to better separate alternative patterns (e.g. the geological features seen in IC1, IC2 and IC3 and the noise pattern seen in IC4). Principal component analysis sorts the data into orthogonal components based on higher variability and tends to mix geological features of interest with noise (PC1, PC2, PC3 and PC4).

In order to accomplish the goal of making an unsupervised seismic facies analysis, we plot the independent components IC1, IC2 and IC3 against a RGB color scheme. As stated before, similar seismic facies are voxels projected to similar colors. In addition, we compare the ICA RGB blending with the PCA RGB blending using PC1, PC2 and PC3.

In Figure 20, we note that the RGB blending using independent components at Horizon A + 196 ms (Figure 20b) provides better resolution of geological features than the RGB blending of principal components (Figure 20a). Like in the individual components, the leveed meandering channels, the tabular shape main channels (green arrows) as well as the small scale geological features such as the older abandoned channel and the oxbows are better delineated using ICA. We also notice, that the ICA RGB blending provides better contrast between distinct seismic facies. While the axis and off-axis of the leveed meandering channel (Posamentier and Kolla, 2003; McHargue et al., 2010; Fildani et al. 2012; Hubbard et al., 2014) are characterized by

similar greenish colors in PCA RGB blending, they are characterized in the ICA RGB blending by a purple color for the axial deposition of the leveed meandering channels and a green color associated with the off-axis to marginal deposition. Moreover, we note that similar to a braided channel, the tabular shape tributary channel has a more variable internal architecture with predominantly purple seismic facies mixed with green and some blue seismic facies. In addition, the oxbows present different infill patterns. Oxbow 1 is filled by a blue, oxbow 2 by a purple and oxbow 3 by a green seismic facies. Finally, the small abandoned channel appears as purple seismic facies.

At Horizon A + 248 ms (Figure 21), the leveed meandering channels 1 and 2 are much better delineated using ICA RGB blending (Figure 21b) than PCA RGB blending (Figure 21a). The leveed meandering channel 1 is characterized predominantly by purple seismic facies intercalated with some blueish seismic facies, while the leveed meandering channels 2 appears as a green seismic facies. As at Horizon A + 196 ms, the tabular shape channel internal architecture is highly variable with a mix of different seismic facies; this variability is better captured using ICA. The distributary channel 1 is characterized by a predominant purple seismic facies, while now the distributary channel 2 looks like a prolongation of the tabular channel because they have the same variable internal architecture. The meandering channel 3 is characterized by a purple seismic facies while oxbow 3 and meandering channel 4 are characterized by a green infill.

In terms of random noise and footprint, ICA RGB blending (Figures 20b and 21b) provides a smoother picture with remarkably less footprint than PCA RGB blending (Figures 20a and 21a). Even though the acquisition footprint in ICA RGB blending increases at Horizon A + 196 ms, we hypothesize that it is associated with independent component 3 (IC3).

ICA shows better results than PCA in terms of delineating deep water architectural elements of interest, reduces noise, and improve the contrast between different seismic facies. However, neither of these techniques can be used to predict thickness or porosity because the independent and principal components project the data onto a mathematical space. To study reflector thickness, we must use the original or reconstructed spectral components (Guo et al., 2009; Zanardo Honorio et al., 2014).

Geological interpretation of seismic facies using ICA RGB blending

Following McHargue et al. (2010), channels associated with turbiditic deposits are a product of multiple waxing and waning flows. During a waxing cycle, high energy turbiditic flows produce erosion forming a channel conduit. In a waning cycle, turbiditic flows become less energetic, thus allowing filling of the channel conduit.

Deposition in deep water channels can be divided into axis, off-axis and margin turbiditic facies (Figure 22). In most cases, the axis represents the thickest part of the channel and is characterized by deposition of thick-bedded amalgamated sandstone facies. In contrast, off-axis to marginal deposition is associated with interbedded sandstone and mudstone facies, also known as heterolytic facies, implying a lower concentration of net sand compared to axis facies (McHargue et al., 2010; Fildani, et al., 2012; Hubbard et al., 2014).

Although the internal architecture of the channels present in the Moki A sands Formation is highly variable and complex, based on principles of geomorphology and following the model of deposition of turbiditic facies (McHargue et al., 2010; Fildani, et al., 2012; Hubbard et al., 2014) and cut-and-fill architecture (Posamentier and Kolla, 2003) in channel complexes, we generate several vertical sections of seismic amplitude through the channels complexes, in order

to correlate the different seismic facies obtained from the ICA RGB blending analysis with axis, off-axis and margin deposition and lateral and upward migration of facies.

In Figure 23a, we generated a vertical section AA' through the straight tabular shape channel that contains a more variable internal architecture of seismic facies with predominantly purple seismic facies mixed with some green and blue facies. We hypothesize that this channel complex was developed as a deep cut associated with high energy turbiditic flows in which, during a waning cycle, weakly unconfined channels migrated inside the channel conduit. According to McHargue, et al. (2010), these weakly unconfined channels are characterized by a tabular shape and similar architecture to braided channels with predominant sand-rich facies. Also, in vertical section AA', we observe the oxbow 3, with a predominant green seismic facies related to low amplitude reflectors, are enclosing the purple seismic facies associated with high amplitude, continuous reflectors.

Vertical section BB' (Figure 23b) through the meandering leveed channel 1 shows an asymmetrical configuration which, according to McHargue et al. (2010), occur in sinusoidal channels. The fact that this channel complex is asymmetrical can be associated with cut-and-fill or waxing and waning cycles (Posamentier and Kolla, 2003). Cut-and-fill architectures can lead to upward and lateral migration of channel facies (Posamentier and Kolla, 2003). We hypothesize that in BB' (Figure 23b) there was a first waxing and waning cycle in which sand-prone facies are deposit in the axis of the channel, while in the off-axis to margin of the channel, mud-prone facies are deposit (Posamentier and Kola, 2003; McHargue et al., 2010). Then, a second waxing-waning cycle occurred, creating a cut-and-fill architecture in which facies migrated upward and laterally (red arrow). On both waxing and waning cycles, sand-prone facies are deposited in the axis of the channel, while mud-prone facies are related to off-axis to

marginal deposition. Also, in vertical section BB', we note that axial facies associated with purple seismic facies are characterized by high amplitude, continuous reflectors with limited lateral extent, while green seismic facies, associated with off-axis to marginal deposition are characterized by low amplitude reflectors. From Figure 23b, we note that the sheet sands of the Moki A sands Formation are represented by a mixture of bright blue with yellow, red and purple seismic facies associated with high amplitude with great lateral extension parallel reflectors.

In Figure 24a, we make another vertical section CC' through meandering leveed channel 1, but now the outer bend of the channel is facing to the opposite direction. In vertical section CC', we note that there is lateral and upward migration of facies (red arrow), thus cut-and-fill architecture related with waxing and waning cycles is present. Like in vertical section BB' (Figure 23b), we hypothesize that sand-prone facies are deposited in the axis of the channel and mud-prone facies deposit in off-axis to marginal deposition. Moreover, purple seismic facies are still associated with axial deposition and characterized by high amplitude continuous reflectors, while green purple facies with low amplitude reflectors represent off-axis to marginal deposits. Sheet sands are associated with bright blue seismic facies, mixed with yellow, red and purple seismic facies.

Vertical section DD' (Figure 24b) through meandering leveed channel 2 shows cut-and-fill architecture associated with waxing-waning cycles. Also, we hypothesize that during channel deposition related with a second waning-waxing cycle, axial deposits from the previous waning-waxing cycle were eroded. Like in previous observations, purple seismic facies represent high amplitude continuous reflectors suggesting sand-prone deposits along the axis of the channel. Furthermore, green seismic facies are still characterized by low amplitude reflectors and they represent mud-prone facies related with off-axis to marginal deposition.

Vertical section EE' (Figure 25) through meandering channel 3 at Horizon A + 248 ms. shows a lateral change in the amplitude thickness which we interpret is associated with differential compaction (Chopra and Marfurt, 2012). Differential compaction is related to lateral changes in lithologies. We interpret the positive relief in EE' as a channel filled with sand-prone sediments that do not experience as much compaction as the mud-prone facies outside it. In this case, the purple seismic facies are associated with sand-prone facies and high amplitude reflectors and the green facies are related to mud-prone sediments and lower amplitude reflectors associated with the Moki B shale Formation.

Based on the observations made using vertical section through the channel complexes present in the Moki A sands Formation, we hypothesize that purple seismic facies, characterized by continuous high amplitude reflectors, are associated with sand-prone facies related to axial deposition. In contrast, we believe that green seismic facies, characterized by low amplitude reflectors, are associated with mud-prone facies related to off-axis to marginal deposition in the meandering channel complexes. Finally, mixed blue, yellow and red facies represent sheet sands deposits, we hypothesize these seismic facies are associated with higher concentration of sand-prone deposits.

Validation of seismic facies using well data

In order to validate our interpretation of the seismic facies using principles of geomorphology and the ICA RGB blending to highlight the different architectural elements, we relate the seismic facies with lithologies analyzing the Gamma Ray log from the Tui SW-2 well. Figure 26 shows that high gamma ray values associated with bathyal claystones of the Moki B shale Formation correlate with the green seismic facies (yellow arrow) suggesting a mud-prone seismic facies. Also the small low gamma ray values (blue arrow) which are associated with

calcareous sandstones, are not seen in the seismic because their thickness is approximately 5 m, thus they are under resolution. In addition, intercalation of high gramma ray with low gamma ray values associated with interbedded calcareous sandstone and claystones related to base of slope turbidites present in the Moki A sands Formation are characterized by red and blue seismic facies (green arrows), which is consistent with our interpretation of sheet sands characterized by a mixture of blue, red and yellow seismic facies. Finally, the low gamma ray calcareous sandstone of approximate thickness of 30 m bracketed by high gamma ray claystone are associated with mixed purple and green seismic facies (orange arrow) in the Tui SW-2 well. Although the Tui SW2 well is not drilled through one of the channel complexes, we believe that the validation of the seismic facies using this well can be extrapolated to the other zones of the seismic volume.

CONCLUSIONS

Applications to a 3D seismic data volume acquired in the Taranaki Basin show that Independent Components Analysis (ICA) are a powerful technique to reduce dimensionality, extract valuable information from multiple seismic attribute volumes and separate geological features from noise. ICA uses higher order statistics that found projections that were more geological and less mathematical than Principal Component Analysis (PCA), where PCs based on Gaussian statistics seems to mix multiple geologic features as well as noise. For this reason, ICA provided better resolution and better footprint reduction than PCA in this study. Small scale geological features characterized by lower reflectivity than large scale geological features are overlooked by the Principal Component Analysis, while in Independent Component Analysis geological features at all scales are well preserved. Specifically, small scale meandering and tabular shape tributary channels as well as abandoned meandering channels and oxbows are

better delineated using ICA. Finally, ICA RGB blending provided better contrast between distinct seismic facies than PCA RGB blending. In ICA RGB blending, axial deposition associated with sand-prone facies is characterized by a distinct (in this case purple color) seismic facies related to high amplitude reflectors. In contrast, off-axis to marginal deposition of the channels is represented by a different (green color) seismic facies associated with mud-prone facies and characterized by low amplitude reflectors. Finally, sheet sand deposits are characterized by high amplitude continuous reflectors with greater lateral extent and are associated with a mixture of (purple, red and yellow) facies dominated by one (bright blue) seismic facies.

ACKNOWLEDGENTS

We thank New Zealand Petroleum and Minerals for providing the Tui3D seismic data to the public for use in research and education. Also, we would like to thank the sponsors of the Attribute Assisted Seismic Processing and Interpretation (AASPI) consortium for their support and to Schlumberger for the licenses in Petrel provided to the University of Oklahoma. We thank Dr. Henry Posamentier, Dr. Lennon Infante, Dr. Richard Brito, Thang Ha and Emilio Torres for their valuable comments.

APPENDIX A

Preprocessing for ICA estimation

Estimation of the independent components $\mathbf{P}=\{\mathbf{P}_1,\mathbf{P}_2\}$ requires finding an unmixing matrix, $\mathbf{W}$, such that its projection maximizes the independence or non-Gaussianity between the components (Hyvärinen and Oja, 2000). ICA assumes that the data have a non-Gaussian distribution. This assumption is valid in seismic data because, according to Walden (1985) and

Zanardo Honorio et al. (2014), seismic data can be considered as super-Gaussian distributions that are characterized by a positive kurtosis.

We apply some preprocessing steps to better condition the problem. Hyvärinen and Oja (2000), suggest subtracting the mean vector $\bar{\mathbf{a}}$ of the data $\mathbf{a}$, from the value at each voxel prior to estimating the independent components. However, unlike human voices and other ICA applications, each seismic attribute may have a different unit of measurement and range of values. For example, the seismic envelope may range between 0 and +10000, while curvature may have value that range between -1 and +1 km^{-1}. For this reason, we apply a Z-score normalization to the data, i.e., subtracting its mean but also dividing by its standard deviation:

$$\mathbf{a}_n^{(\mathrm{norm})}=(\mathbf{a}_\mathrm{n} - \overline{\mathbf{a}_\mathrm{n}})/\sigma(\mathbf{a}_\mathrm{n}). \quad \text{(A1)}$$

The next preprocessing step is to whiten the data. Whitening guarantees that the data are uncorrelated (mathematically, its covariance matrix is the identity matrix). The correlation matrix, $\mathbf{C}$, is constructed by comparing each sample vector to itself and all its neighbors and can be computed from K attribute volumes as:

$$C_{kl} = \frac{1}{M}\sum_{m=1}^{M} \mathrm{a}_{mk}^{(\mathrm{norm})}(t_m, x_m, y_m)\mathrm{a}_{ml}^{(\mathrm{norm})}(t_m, x_m, y_m), \quad \text{(A2)}$$

where M is number of voxels in the volume to be analyzed.

According to Hyvärinen and Oja (2000), uncorrelated data simplify the estimation of independent components because the mixing matrix $\mathbf{A}$ becomes an orthogonal matrix, thereby reducing the number of free parameters to be computed.

Principal Component Analysis (PCA) is a common technique used for dimensionality and noise reduction. The k^{th} principal component, $\mathbf{P}^{(\mathrm{k})}$, at the m^{th} voxel $(t_m,,x_m,y_m)$ is a scalar that

represents the projection of a N-dimensional sample vector, $\mathbf{a}$, against the k^{th} unit length, N-dimensional eigenvector, $\mathbf{v}^{(k)}$:

$$\boldsymbol{P}_n^{(k)}(t_m, x_{m,} y_m) = \sum_{n=1}^{N} \mathbf{a}_n^{(\text{norm})}(t_m, x_{m,} y_m)\boldsymbol{v}_n^{(k)}. \quad \text{(A3)}$$

PCA can be used to whiten the data. Specifically, after computing the principal components, $\mathbf{P_n}$, we rescaled them by $1/\sqrt{\lambda_n}$ thereby making each of the projections have unit variance:

$$\mathbf{a}_n^{(w)} = \frac{\boldsymbol{P}_n^{(k)}(t_m, x_{m,} y_m)}{(\lambda_n + \varepsilon)^{1/2}}, \quad \text{(A4)}$$

where, $\mathbf{a_n^{(w)}}$, represents the data after Z-score normalization and whitening, λ_n are the eigenvalues of the correlation matrix, and ε is a fraction of the largest eigenvalue λ_1 , to avoid division by zero.

Using PCA whitening, we not only reduce the dimensionality of the data but we also reduce noise during the independent component estimation (Hyvärinen and Oja, 2000). To decide how many components we should preserve, we analyze the percentage of variance retained (Stanford, 2018).

If we have N principal components the eigenvalues are $\lambda_1, \lambda_2, \lambda_3, \ldots, \lambda_N$ where $\lambda_n \geq \lambda_{n+1}$. For N attributes, Stanford (2018) suggests keeping the largest K components whose sum just exceeds a user-defined percentage β, of the variability E of the data, where the remaining variability is considered to be noise:

$$\frac{\sum_{n=1}^{K} \lambda_n}{\sum_{n=1}^{N} \lambda_n} \geq \beta, \quad \text{(A5)}$$

where we use a value $\beta = 0.9$ to define the data from noise.

The ICA algorithm

Based on the Central Limit Theorem, Hyvärinen and Oja (2000), state that the distribution of two independent variables is less Gaussian than the distribution of the sum of the two variables. Therefore, by maximizing the non-Gaussianity of the preprocessed data, we can find the unmixing matrix, **W**, that maximizes the independence of the sources $\mathbf{P_1}$ and $\mathbf{P_2}$.

Because a Gaussian variable has the largest entropy of all, Hyvärinen and Oja (2000), quantitatively measure non-Gaussianity based on an approximation of negentropy, which is a modified version of entropy that is always nonnegative and is equal to zero for a Gaussian distribution.

Assuming a random variable $\mathbf{y}=\mathbf{W}^{\mathrm{T}}\mathbf{a}^{(\mathrm{w})}$ with zero mean and unit variance, Hyvärinen (1999) approximate the negentropy J as:

$$J(y) = \{E[G(y)] - E[G(v)]\}^2, \tag{A6}$$

where G is a non-quadratic function called the contrast function, v is a centered and whitened Gaussian variable and E is the expected value operator. In practice, the expectation operator must be replaced by the sample means (Hyvärinen and Oja, 2000).

To compute the independent components, Hyvärinen and Oja (2000), developed an algorithm called "FastICA", where, the goal is to maximize the contrast function, G. Any non-quadratic function can be used in the computations (Hyvärinen and Oja, 2000). We follow Zanardo Honorio et al. (2014), and use the contrast function:

$$G(y) = -e^{-\left(y^2/2\right)}, \tag{A7}$$

which through empirical analysis appears to provide good resolution and delineation of the geological features. The independent components are computed simultaneously. To avoid convergence to the same maxima, the outputs are decorrelated after each iteration (Hyvärinen and Oja, 2000).

Following Hyvärinen and Oja (2000), in each iteration of the algorithm, we update each row of the unmixing matrix, **W**, is updated by

$$\mathbf{W}_j^+ = E\left[\mathrm{a}^{(w)}\frac{\partial G}{\partial y}\left(\mathbf{W}_j^T\mathbf{a}^{(w)}\right)\right] - E\left[\frac{\partial^2 G}{\partial^2 y}\left(\mathbf{W}_j^T\mathbf{a}^{(w)}\right)\right]\boldsymbol{W}_j, \tag{A8}$$

and normalized by:

$$\mathbf{W}_j^+ = {\mathbf{W}_j^+}\Big/{||\mathbf{W}_j^+||}, \tag{A9}$$

where $\mathbf{W}^+$ is the updated unmixing matrix Finally, the updated unmixing matrix, $\mathbf{W}^+$, is decorrelated using Eigenvalue Decomposition (EVD) by

$$\mathbf{W}_{\mathrm{decorr}}^+ = (\mathbf{W}\mathbf{W}^{\mathbf{T}})^{-1/2}\mathbf{W}. \tag{A10}$$

Convergence is reached when the dot-product between the old and new values of W is close to 1, indicating that they are parallel and unchanged. (Hyvärinen and Oja, 2000).

Finally, the energy of each independent component is the sum of the energy over all the voxels that fall in the target region:

$$L = \sum_{m=1}^{M} y_i\left(t_m, x_{m,} y_m\right)^2. \tag{A11}$$

where, $y_i\left(t_m, x_{m,} y_m\right)$ is the i^{th} independent component at voxel m, and M is the number of voxels in the target area.

REFERENCES

Bussell, M.R., 1994, Seismic interpretation of the Moki Formation on the Maui 3D survey, Taranaki Basin: New Zealand Petroleum Conference Proceedings, Ministry of Economic Development, 240-255.

Chopra, S., and K.J. Marfurt, 2012, Seismic attribute expression of differential compaction: 82nd Annual International Meeting, SEG, Expanded Abstract, 1-5.

Chopra, S., and K.J. Marfurt, 2014, Churning seismic attributes with principal component analysis: 84th Annual International Meeting, SEG, Expanded Abstract, 2672-2676

Chopra, S., and K.J. Marfurt, 2015, Choice of mother wavelets in CWT spectral decomposition: 85th Annual International Meeting, SEG, Expanded Abstract, 2957-2961.

Chopra, S., and K.J. Marfurt, 2016, Spectral decomposition and spectral balancing of seismic data: The Leading Edge, **35**, 176-179, doi: 10.1190/tle35020176.1.

Coléou, T., M. Poupon, and K. Azbel, 2003, Unsupervised seismic facies classification: A review and comparison of techniques and implementation: The Leading Edge, **22**, 942–953, http://dx.doi.org/10.1190/1.1623635.

Dauzacker, M.V., J.S. Yang, G.A. Pomilio, and V.S. Till, 1996, A new exploratory approach to the Moki-Manaia oil discoveries: New Zealand Petroleum Conference Proceedings, 86-104.

De Bock, J.F., 1994, Moki Formation, a Miocene reservoir sequence, its facies distribution and source in offshore, southern Taranaki Basin: New Zealand Petroleum Conference

Proceedings, 155-167.

Engbers, P., 2002, Evaluation of Moki sands prospectivity in Maui PML: New Zealand Petroleum Conference Proceedings, Ministry of Economic Development.

Fildani A., S. M. Hubbard, J.A. Covault, K. L. Maier, B.W. Romans, M. Traer, and J.C. Rowland, 2012, Erosion at inception of deep-sea channels: Marine and Petroleum Geology, **41**, 48-61, doi:10.1016/j.marpetgeo.2012.03.006

Guo, H., K. J. Marfurt, and J. Liu, 2009, Principal component spectral analysis: Geophysics, **74**, no. 4, 35–43, doi: 10.1190/1.3119264.

Hansen, R. J., and P. J. Kamp, 2006, An integrated biostratigraphy and seismic stratigraphy for the late Neogene continental margin succession in northern Taranaki Basin, New Zealand: New Zealand Journal of Geology and Geophysics, **49**, no. 1, 39–56.

Hubbard S.M., J.A. Covault, A. Fildani, and B.W. Romans, 2014, Sediment transfer and deposition in slope channels: Deciphering the record of enigmatic deep-sea processes from outcrop: Geological Society of America Bulleting, **126**, no.5-6, 857-871, doi: 10.1130/B30996.1

Hyvärinen, A., 1999, Survey of independent component analysis: Neural Computing and Applications, **2**, 94–128.

Hyvärinen, A., and E. Oja, 2000, Independent Component Analysis: Algorithms and Applications: Neural Networks, **13**, nos. 4-5, 411-430.

Infante-Paez, L., and K. Marfurt, 2017, Seismic expression and geomorphology of igneous bodies: A Taranaki Basin, New Zealand, case study: Interpretation, **5**, no. 3, 121-140.

Infante-Paez, L., 2018, Seismic expression of igneous bodies in sedimentary basins and their impact on hydrocarbon exploration: Examples from a compressive tectonic setting, Taranaki Basin, New Zealand: PhD. Dissertation, University of Oklahoma.

King, P. R., G. H. Scott, and P. H. Robinson, 1993, Description, correlation and depositional history of Miocene sediments outcropping along North Taranaki coast: Institute of Geological & Nuclear Sciences Ltd., p. 199.

King, P. R., and G. P. Thrasher, 1996, Cretaceous Cenozoic geology and petroleum systems of the Taranaki Basin, New Zealand: Institute of Geological & Nuclear Sciences 2.

Kohonen, T., 1982, Self-organized formation of topologically correct feature maps: Biological Cybernetics, **43**, 59–69, doi: 10.1007/BF00337288.

Li, F., and W. Lu, 2014, Coherence attribute at different spectral scales: Interpretation, **2**, no. 1, SA99–SA106, http://dx.doi. org/10.1190/INT-2013-0089.1.

Li, Y., Zheng, X., Li, J., 2009, Dimensionality reduction and feature extraction from seismic spectral decomposed data using independent component analysis: CPS/SEG Beijing 2009 International Geophysical Conference & Exposition.

Li, F., J. Qi, B. Lyu, and K. J. Marfurt, 2018, Multispectral coherence: Interpretation, **6**, no. 1, T61-T69, doi: 10.1190/INT-2017-0112.1.

Lubo-Robles, D., and K. J. Marfurt, 2017, Delineation of thick incised canyons using spectral-decomposition analysis, curvature and Self-Organizing Maps in the Exmouth Plateau, Australia: 87th Annual International Meeting, SEG, Expanded Abstract, 2420-2424.

MacQueen, J., 1967, Some methods for classification and analysis of multivariate observations: Proceedings of the Fifth Berkeley Symposium on Mathematical Statistics and Probability, University of California Press, **1**, 281–297.

Marfurt, K. J., and R.L. Kirlin, 2001, Narrow-band spectral analysis and thin-bed tuning: Geophysics, **66**, 1274–1283.

Marfurt, K.J., 2018, Seismic attributes as the Framework for Data Integration Throughout the Oilfield Life Cycle: Distinguished instructor series, No. 21.

McHargue T., M.J. Pyrcz, M.D. Sullivan, J.D. Clark, A. Fildani, B.W. Romans, J.A. Covault, M. Levy, H.W. Posamentier, and N.J. Drinkwater, 2010, Architecture of turbidite channel systems on the continental slope: Patterns and predictions: Marine and Petroleum Geology, **28**, 728-743, doi: 10.1016/j.marpetgeo.2010.07.008.

Palmer, J, 1985, Pre-Miocene lithostratigraphy of Taranaki Basin, New Zealand: New Zealand Journal of Geology and Geophysics, **28,** no 2.,197-216.

Pilaar, W.F.H, and L.L. Wakefield, 1984, Hydrocarbon generation in the Taranaki Basin, New Zealand: AAPG Special Volumes M35, Petroleum Geochemistry and Basin Evaluation, 405-423.

Posamentier, H.W., V. Kolla, 2003, Seismic geomorphology and stratigraphy of depositional elements in deep-water settings. Journal of Sedimentary Research 73, 367-388.

Partyka, G., J. Gridley, and J. Lopez, 1999, Interpretational applications of spectral decomposition in reservoir characterization: The Leading Edge, **18**, no. 3, 353-360, doi: 10.1190/1.1438295.

Roden, R., T. Smith, and D. Sacrey, 2015, Geologic pattern recognition from seismic attributes: Principal component analysis and self-organizing maps: Interpretation, **4**, SAE59–SAE83, S. http://dx.doi.org/10.1190/INT-2015-0037.1.

Roy, A., S. R. Araceli, J. T. Kwiatkowski, and K. J. Marfurt, 2014, Generative topographic mapping for seismic facies estimation of a carbonate wash, Veracruz Basin, Southern Mexico: Interpretation, **2**, no. 1, SA31–SA47, doi: 10.1190/INT-2013-0077.1.

Sinha S., P. Routh, P. Anno, and J. Castagna, 2005, Spectral decomposition of seismic data with continuous-wavelet transform: Geophysics, **70**, no. 6, 19-25.

Sinha, S., D. Devegowda, B. Deka, 2016, Multivariate Statistical Analysis for Resource Estimation in Unconventional Plays Application to Eagle Ford Shales: Society of Petroleum Engineers, doi: 10.2118/184050-MS.

Stanford, 2018, PCA Whitening: http://ufldl.stanford.edu/tutorial/unsupervised/PCAWhitening/. Accessed on March 26th, 2018.

Strecker, U., and R. Uden, 2002, Data mining of 3D post- stack attribute volumes using Kohonen self-organizing maps: The Leading Edge, **21**, 1032–1037, http://dx.doi.org/10.1190/1.1518442.

Thrasher, G., 1992, Late Cretaceous geology of Taranaki Basin, New Zealand: PhD. Dissertation, Victoria University of Wellington.

Thrasher, G. P., B. Leitner, and A. W. Hart, 2002, Petroleum system of the Northern Taranaki Graben: New Zealand Petroleum Conference Proceedings, Ministry of Economic Development.

Tibaduiza, D.A., L.E., Mujica, M. Anaya, J. Rodellar, and A. Güemes., 2012, Principal Component Analysis vs. Independent Component Analysis for Damage Detection: 6th European Workshop on Structural Health Monitoring.

Veritas DGC, Australia Pty. Ltd / New Zealand Overseas Petroleum Ltd, 2003, Tui-3D seismic survey: Ministry of Economic Development New Zealand, Unpublished Petroleum Report, PR2830.

Walden, A.T., 1985, Non-Gaussian reflectivity, entropy, and deconvolution: Geophysics, **50**, no.12, 2862–2888, doi: 10.1190/1.1441905.

Yagci, G., 2016, 3D seismic structural and stratigraphic interpretation of the Tui-3D field, Taranaki Basin, New Zealand: Master's Thesis, Missouri University of Science and Technology.

Zhao, T., V. Jayaram, A. Roy, and K.J. Marfurt, 2015, A comparison of classification techniques for seismic facies recognition: Interpretation, **3**, no. 4, SAE29-SAE58, doi: 10.1190/INT-2015-0044.1

Zhao, T., Li F., Marfurt, K. J., 2016, Advanced self-organizing map facies analysis with stratigraphic constraint: 86th Annual International Meeting, SEG, Expanded Abstract, 1666-1670

Zanardo Honorio, B., A. Sanchetta, E. Pereira, and A. Vidal, 2014, Independent component spectral analysis: Interpretation, **2**, SA21-SA29, doi: 10.1190/INT-2013-0074.1.

CAPTIONS

Figure 1. Illustration of Independent Component Analysis (ICA) using the popular cocktail-party problem. The goal is to recover the individual signals $\mathbf{P_1}$ and $\mathbf{P_2}$ from the mixtures signals $\mathbf{X_1}$ and $\mathbf{X_2}$.

Figure 2. Differences between Principal Component Analysis (PCA) and Independent Component Analysis (ICA). Attributes $\boldsymbol{a_1}$ and $\boldsymbol{a_2}$ are scaled by their means and standard deviations. The first eigenvector $\mathbf{v_1}$ is a line that least-squares fits the data cloud and best represent the variance of the data. PC1 is a projection of each data point onto $\mathbf{v_1}$. The second eigenvector $\mathbf{v_2}$ is a perpendicular to $\mathbf{v_1}$ and for two dimensions these two eigenvectors best represents the data. In contrast, the independent components IC1 and IC2 are latent variables whose order is undefined and are not orthogonal to each other (Hyvarinen and Oja, 2000; Tibaduiza et al., 2012). To compute the independent components, each data point is projected onto the whitened eigenvectors $\mathbf{v_1}$ and $\mathbf{v_2}$, and then projected onto the unmixing matrix $\mathbf{W}$.

Figure 3. Independent Component Analysis (ICA). The algorithm is a based on the FastICA algorithm developed by Hyvarinen and Oja (2000), but with modifications for volumetric seismic attribute application.

Figure 4. The Taranaki Basin can be divided in the Taranaki Graben Complex and the Western Platform (Pilaar and Wakefiled, 1984). The Tui3D seismic survey (orange star) is situated offshore Taranaki Basin, New Zealand. After King et al. (1993), King and Thrasher (1996), Thrasher et al. (2002) and Hansen and Kamp (2006).

Figure 5. Analysis interval between Horizon A and Horizon B enclosing the Moki Formation. A strong continuous reflector associated with the Tikorangi Limestone was picked and phantom horizons were created bracketing the Moki Formation. In order to completely enclose the channel complexes present in the Moki A sands Formation, the analysis interval brackets the Moki A sands Formation, the Moki B Shale and parts of the Moki B sands and Upper Manganui. The analysis interval has a width of 300 ms.

Figure 6. Spectral magnitude, independent and principal components volumes are flattened against the top analysis interval Horizon A. This procedure is similar that extracting them along phantom horizons within the analysis interval.

Figure 7. Spectral magnitude components plotted against a RGB color scheme along a phantom Horizon A + 196 ms. (a) Combination of 25-35-45 Hz spectral magnitude components showing the channel complexes present in the Moki A sands Formation. (b) The combination of 40-50-60 Hz also shows the channel complexes, however the small scale abandoned meandering channel (blue arrow) is better resolved in the combination of 25-35-45 Hz. (c) Combination 60-70-80 Hz. At higher frequencies, the picture is contaminated by acquisition footprint (red rectangle). Internal architecture of the channel is still delineated (yellow arrows) (d) Combination of the 25-

50-75 Hz. Infill of the channels predominantly tune at lower frequencies than their flanks (~50 Hz). Thin beds inside the channels tune at approximately 75 Hz.

Figure 8. Spectral magnitude components plotted against a RGB color scheme along a phantom Horizon A + 248 ms. Analyzing the same combinations as in Figure 7, the infill of the channels still tunes at lower frequencies while the flanks, internal thin beds and acquisition footprint tune at higher frequencies.

Figure 9. Proposed workflow to highlight and study the internal architecture of the channel complexes present in the Moki A sands Formation. We use spectral magnitude components ranging from 25 to 80 Hz with intervals of 5 Hz to analyze the stratigraphy and depositional system of the target area. Independent Component Analysis (ICA) attempts to extract stronger correlated patterns in the data (geology and acquisition footprint), with random uncorrelated noise remaining in the residual. The independent components are sorted by visual inspection using geological insight. For both PCA and ICA we co-render the three most useful components using RGB blending.

Figure 10. Variability retained. (a) Based on the percentage of variability retained (Stanford, 2018), the algorithm automatically outputs four components during the PCA whitening preprocessing step that represent 94.04% of the variability of the data, from these components the independent components are computed. Also, PC1 is the strongest and represent 63.52% of the variability (b) PC1 is characterized by a flat spectrum because the spectral components were spectrally balanced. PC2 monotonically changes from lower to higher frequencies and is orthogonal to PC1. PC3 is orthogonal to PC1 and PC2 and its spectrum changes sign between 45 to 50 Hz. PC4 captures 5.74% of the variability and is orthogonal to PC1, PC2 and PC3. Little physical significance can be assigned to the eigenspectrum because principal components reside

in a mathematical space where spectral components are represented as orthogonal uncorrelated components.

Figure 11. ICA energy. (a) Independent components exhibit similar energy and this is not clearly correlated to geology, thus independent components are sorted based on visual inspection, seeking for better resolution of large and small scale geological features (b) IC1 captures 23.92% of the energy and tend to represent lower frequency geological features. IC2 amplitude is higher at frequencies from 30 to 60 Hz. IC3 captures the largest energy and its spectrum is associated with low to moderate frequencies. IC4 spectrum monotonically changes from lower to higher frequencies. Because independent components represent spectral components as oblique projections seeking for independence, the ICA spectra has more physical significance than the PCA eigenspectrum.

Figure 12. Principal component 1 (PC1) vs. independent component 1 (IC1) along phantom Horizon A + 196 ms. (a) PC1 shows the confluence (red arrow) of two leveed meandering tributary channels with moderate sinuosity and a tabular shape channel with an architecture similar to a braided channel (green arrows). In addition, PC1 is contaminated by acquisition footprint (red rectangle) (b) IC1 shows a smoother, less noise picture with less acquisition footprint (red rectangle) than PC1. Also, in IC1 the large-scale geological features (green arrows) and the small-scale geological features such as oxbows (orange arrows) and a small abandoned meandering channel (blue arrow) are better delineated than in PC1. Please, note that numbering is used to identify the different architectural elements and is not associated with time of deposition of the channel complexes.

Figure 13. Principal component 1 (PC1) vs. independent component 1 (IC1) along Horizon A + 248 ms. (a) The leveed meandering channel (green arrows) are difficult to delineate using PC1,

also PC1 is still contaminated by acquisition footprint (red rectangle). (b) IC1 provides better resolution than PC1, thus the leveed meandering channels (green arrows) are better delineated using the former. In addition, IC1 has less footprint (red rectangle) than PC1 and the internal architecture of the tabular shape channel improves considerably. Finally, the small scale oxbow (orange arrow) that is not seen in PC1 can be interpreted using IC1.

Figure 14. Principal component 2 (PC2) vs. independent component 2 (IC2) along Horizon A + 196 ms. (a) PC2 is characterized by strong acquisition footprint (red rectangle), also the large scale leveed meandering and tabular channels (green arrows) and the small scale geological features such as oxbows (orange arrows) and the small abandoned channel (blue arrow) are difficult to interpret using PC2. (b) IC2 provides a remarkable increase in the resolution compared to PC2, thus the large scale (green arrows) and small scale geological features (orange arrows and blue arrows) are easier to delineate in IC2. In addition, the independent component 2 has less acquisition footprint (red rectangle) than the principal component 2. Similar to Figures 12 and 13, numbering is used to identify the different architectural elements and is not associated with time of deposition of the channel complexes.

Figure 15. Principal component 2 (PC2) vs. independent component 2 (IC2) at phantom Horizon A + 248 ms. (a) In PC2, the leveed meandering channels 1, 2 and 4 (green arrows) are difficult to interpret, also the principal component 2 is characterized by acquisition footprint (red rectangle) and random noise. (b) In contrast, IC2 provides a result with less acquisition footprint (red rectangle) and random noise compared to PC2. Moreover, the leveed meandering channels (green arrows) that were difficult to interpret in PC2 are better delineated using IC2. The small scale oxbow (orange arrow) is also better resolved in IC2.

Figure 16. Principal component 3 (PC3) vs. independent component 3 (IC3) at Horizon A + 196 ms. (a) From PC3 is possible to interpret the large scale geological features such as the leveed meandering channels and the subsequent merged main channel (green arrows) and the small scale oxbows (orange arrows). Also, the small abandoned meandering (blue arrow) channel that was not possible to delineate in PC1 and PC2 is now seen in PC3 (b) IC3 is characterized by less acquisition footprint (red rectangle) and smoother results than PC3. Also, the large scale (green arrows) and small scale (orange arrows) geological features are well delineated. However, the small abandoned meandering channel (blue arrow) was not completely delineated in IC3. Similar to the previous analysis, numbering is used to identify the different architectural elements and is not associated with time of deposition of the channel complexes.

Figure 17. Principal component 3 (PC3) vs. independent component 3 (IC3) along phantom Horizon A + 248 ms. (a) The resolution of the leveed meandering and the tabular channels (green arrows) increases considerably in PC3, thus is easier to interpret the geological features. Also, is possible to observe acquisition footprint (red rectangle) in PC3. (b) Although the resolution of the large geological features increased in PC3, they are still better delineated using IC3. Moreover, IC3 still provides a smoother picture with less acquisition footprint (red rectangle) than PC3. The small scale oxbow (orange arrow) can be interpreted on both pictures, but its resolution seems to be greater in PC3.

Figure 18. Principal component 4 (PC4) vs. independent component 4 (IC4) along Horizon A + 196 ms. (a) In PC4, geological deep water architectural elements can still be interpreted, but they are not as well delineated as in the other principal components. In addition, PC4 still presents acquisition footprint (red rectangle) and random noise as in PC1, PC2 and PC3. (b) IC4 is

characterized by strong acquisition footprint and random noise. Architectural elements are difficult to delineate.

Figure 19. Principal component 4 (PC4) vs. independent component 4 (IC4) at phantom Horizon A + 248 ms. (a) PC4 is still contaminated by acquisition footprint (red arrow) and random noise, but large (green arrows) and small scale (orange and blue arrows) geological features are interpreted. (b) IC4 is still contaminated by strong acquisition footprint and random noise. Large and small scale geological features are difficult to interpret. We hypothesize that because independent component analysis looks for independence in the multivariate data, it provides better separation between geological features (IC1, IC2 and IC3) and noise signal (IC4) than PCA. Also, independent components provides better resolution of large and smaller scale geological features than principal component analysis, thus providing a mean of making a better seismic interpretation.

Figure 20. RGB blending of PC1, PC2 and PC3 vs. RGB blending of IC1, IC2 and IC3 at phantom Horizon A + 196 ms, in which similar colors can be interpreted as similar seismic facies. (a) From PCA RGB blending is possible to analyze the large scale geological features (green arrows), and the small scale oxbows (orange arrows), but the small abandoned channel (blue arrow) is only partially delineated. PCA RGB blending is contaminated by acquisition footprint (red rectangle). Axis and off-axis seismic facies are characterized by similar greenish colors. (b) From ICA RGB blending the large scale (green arrows) and small scale geological features such as oxbows (orange arrows) and the small abandoned channel (blue arrow) are better delineated than PCA RGB blending. In addition, the former presents lower acquisition footprint (red rectangle) and random noise than the latter. ICA RGB blending also provides a better contrast between different seismic facies, e.g., the axis of the channel is characterized with

a purple seismic facies, while the off-axis of the channel is associated with a green seismic facies. Also, the tabular shape channel is characterized by a more variable internal architecture with predominant purple seismic facies mixed with blue and green seismic facies. Finally, the oxbows infill varies from purple to blue and green facies and the small abandoned channel is associated with purple seismic facies.

Figure 21. RGB blending of PC1, PC2 and PC3 vs. RGB blending of IC1, IC2 and IC3 at phantom Horizon A + 248 ms, similar colors are associated with similar seismic facies. (a) From PCA RGB blending, the large scale meandering and tabular shape channels are well delineated but the resolution decreases compared to the ICA RGB blending. Also, the former presents more acquisition footprint than the latter. (b) The geological architectural elements are better resolved in ICA RGB blending than in PCA RGB blending. The leveed meandering channel 1 is characterized predominantly by purple seismic facies intercalated with some blueish seismic facies, and the leveed meandering channels 2 is associated with a green seismic facies. The tabular shape channel internal architecture is highly variable with a mix of different seismic facies. The distributary channel 1 is characterized by a predominant purple seismic facies and the distributary channel 2 looks like a prolongation of the tabular channel. Finally, the meandering channel 3 is characterized by only a purple seismic facies and the oxbow 3 and the meandering channel 4 are characterized by a greenish infill.

Figure 22. Following McHargue et al. (2010); Fildani, et al. (2012) and Hubbard et al., (2014), deposition of turbiditic facies in deep water channels can be divided into axis, off-axis and margin. In general, the axis of the channel represents the thickest part and is associated with deposition of thick-bedded amalgamated sandstone facies. Off-axis to marginal deposition is

characterized by interbedded sandstone and mudstone facies (heterolytic facies), implying a lower concentration of net sand. Picture after McHargue et al. (2010) and Hubbard et al. (2014).

Figure 23. Geological interpretation of seismic facies using ICA RGB blending and principles of geomorphology of architectural elements in deep water channel complexes. (a) Vertical section AA' intersecting the straight tabular-shape channel characterized by a more variable internal architecture with predominantly purple seismic facies mixed with some green and blue facies. We interpret that this tabular shape channel was developed as a deep cut related to high energy turbiditic flows during a waning cycle. Also, weakly unconfined channels migrated inside the channel conduit. These weakly unconfined channels are characterized by a tabular shape and similar architecture to braided channels with predominant sand-rich facies. The oxbow 3, with a predominant green seismic facies associated with low amplitude reflectors encloses purple seismic facies related to high amplitude, continuous reflectors. (b) Vertical section BB' through the meandering leveed channel 1. The sinusoidal channel is characterized by an asymmetrical configuration, which is associated with cut-and-fill architecture. We interpret two different waxing and waning cycles in which sand-prone facies, characterized by high amplitude reflectors, are deposited in the axis of the channel, while mud-prone facies, associated with low amplitude reflectors, are related to off-axis to marginal deposition. Also, upward and lateral migration of channel facies is seen (red arrow). Sheet sands are associated with a mixture of bright blue with yellow, red and purple seismic facies related to high amplitude with great lateral extension parallel reflectors.

Figure 24. Geological interpretation of seismic facies using ICA RGB blending and principles of geomorphology of architectural elements in deep water channel complexes. (a) Vertical section CC' intercepting the meandering leveed channel 1, with the outer bend of the channel facing to

the opposite direction compared to BB'. Cut-and-fill architectures, associated with lateral and upward migration of facies (red arrow), are interpreted. Similar to vertical section BB', we interpret sand-prone facies are deposited in the axis of the channel and are characterized by purple seismic facies associated with high amplitude continuous reflectors. Mud-prone facies deposit in off-axis to marginal deposition are related to green purple facies characterized by low amplitude reflectors. Finally, sheet sands are associated with bright blue seismic facies, mixed with yellow, red and purple seismic facies. (b) Vertical section DD' through the meandering leveed channel 2. Cut-and-fill architectures associated with waxing-waning cycles are interpreted. We hypothesize that during channel deposition related with a second waning-waxing cycle, axial deposits from the previous waning-waxing cycle were eroded. Purple seismic facies represent high amplitude continuous reflectors, which based on geomorphology concepts, we believe are associated with sand-prone deposits along the axis of the channel. Green seismic facies are related to low amplitude reflectors and represent mud-prone facies associated with off-axis to marginal deposition.

Figure 25. Geological interpretation of seismic facies using ICA RGB blending and principles of geomorphology of architectural elements in deep water channel complexes. Vertical section EE' through meandering channel 3 at Horizon A + 248 ms. There is a lateral change in the amplitude thickness which is related to differential compaction (Chopra and Marfurt, 2012). Differential compaction is associated with lateral changes in lithologies. In this case, we interpret the positive relief as a channel filled with sand-prone sediments related to purple seismic facies, that do not experience as much compaction as the mud-prone facies of the Moki B shale Formation, associated with green seismic facies, outside it.

Figure 26. Validation of the interpretation, based on principles of geomorphology, of the seismic facies in the Moki A sands Formation using the Gamma Ray log from the Tui SW-2 well. High gamma ray values associated with bathyal claystones of the Moki B shale Formation are associated with the green seismic facies (yellow arrow) which in our interpretation, we hypothesized were associated with mud-prone seismic facies. Small low gamma ray values (blue arrow) associated with calcareous sandstones are not seen in the seismic because they are under resolution. Intercalation of high and low gramma ray values associated with interbedded calcareous sandstone and claystones related to base of slope turbidites of the Moki A sands Formation are associated with red and blue seismic facies (green arrows), this correlate with our interpretation of sheet sands characterized by a mixture of blue, red and yellow seismic facies. The low gamma ray calcareous sandstone of thickness approximate to 30 m bracketed by high gamma ray values associated with bathyal claystones are related with mixed purple and green seismic facies (orange arrow).

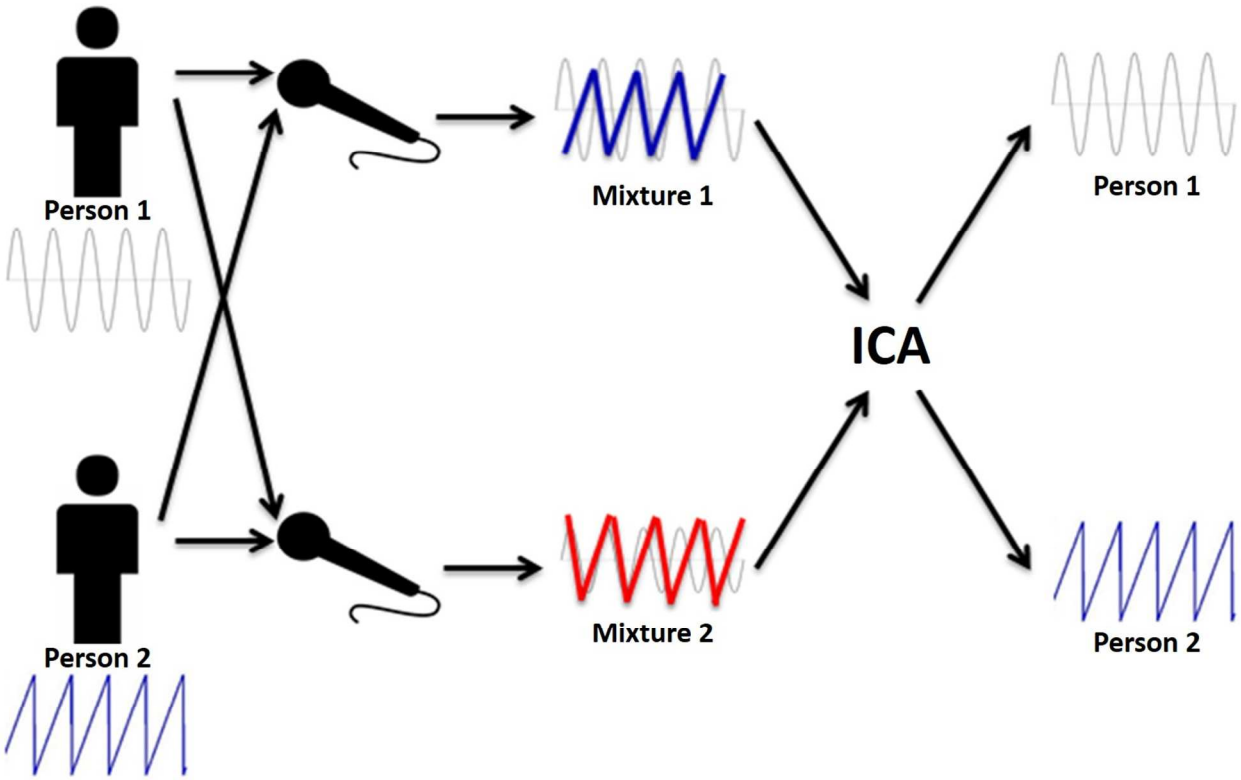

Figure 1.

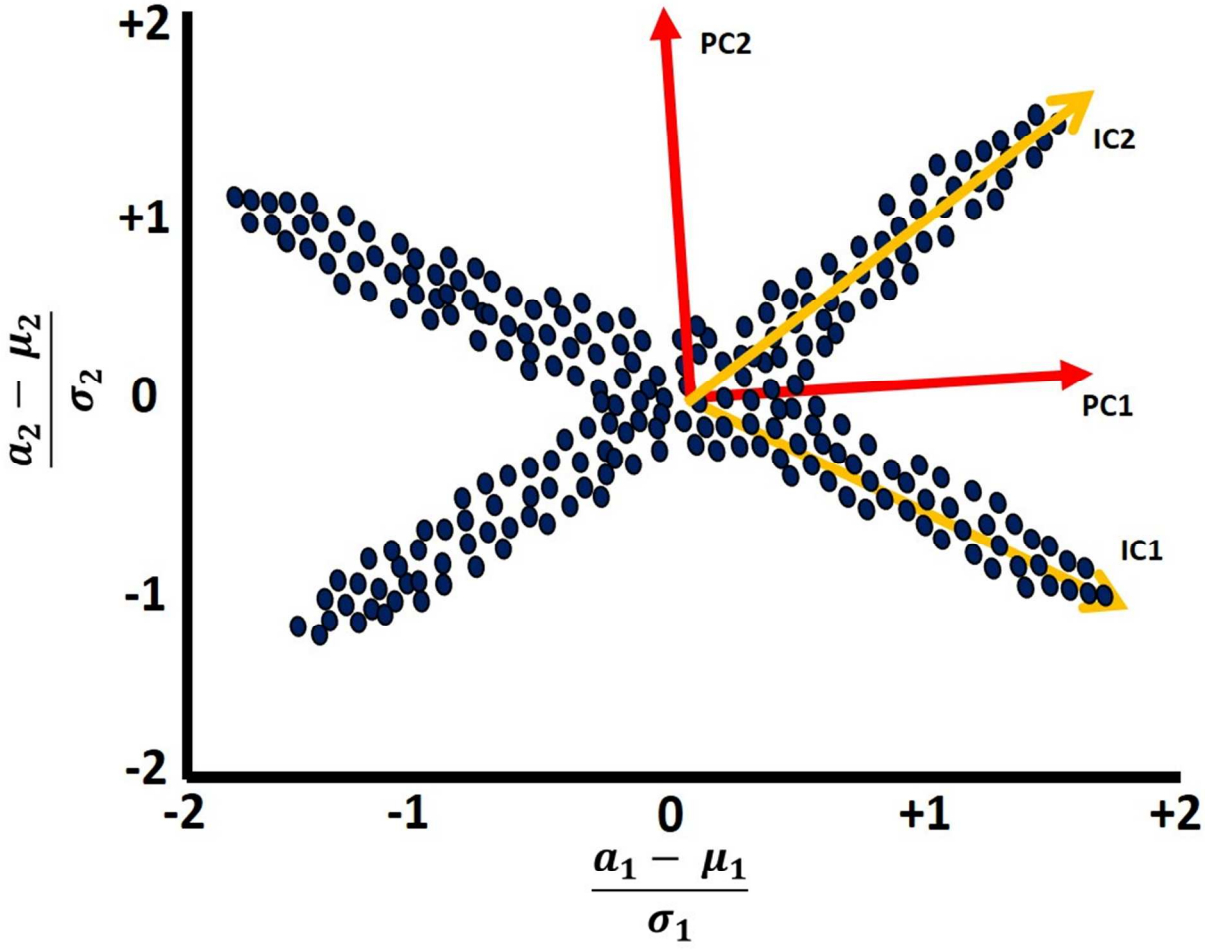

Figure 2.

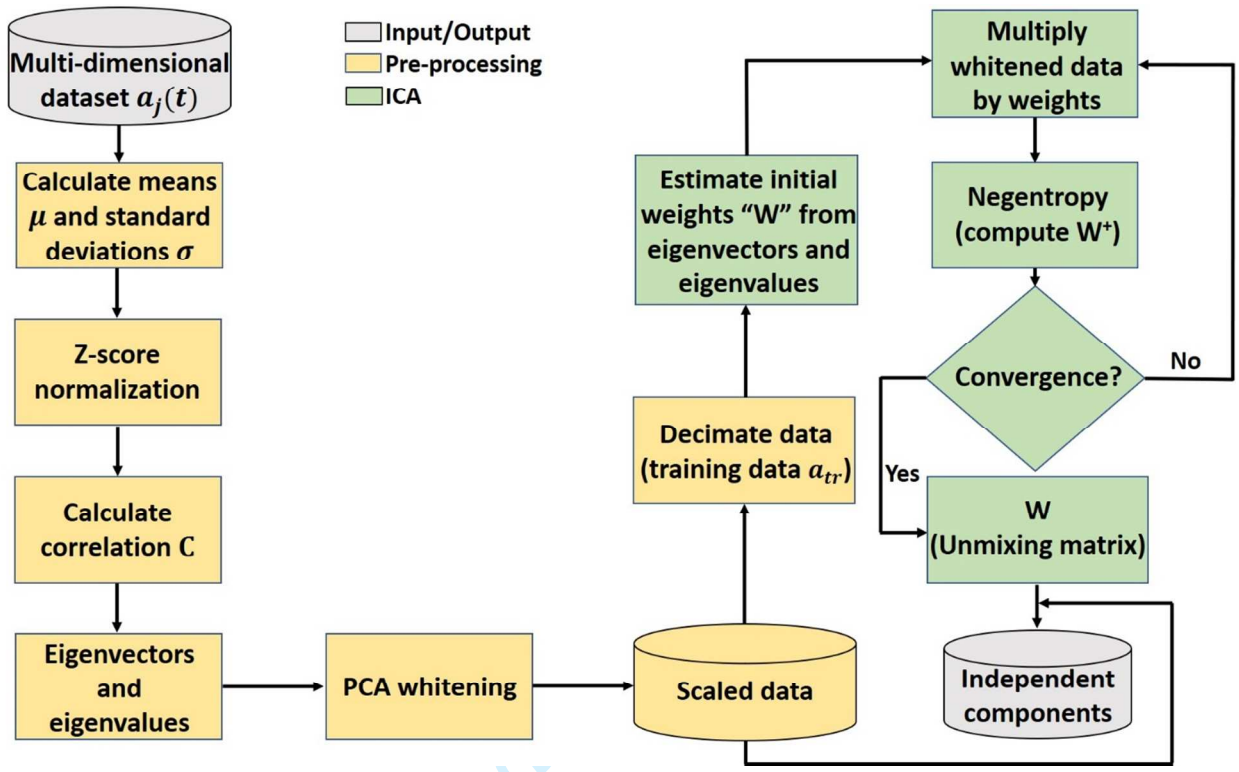

Figure 3.

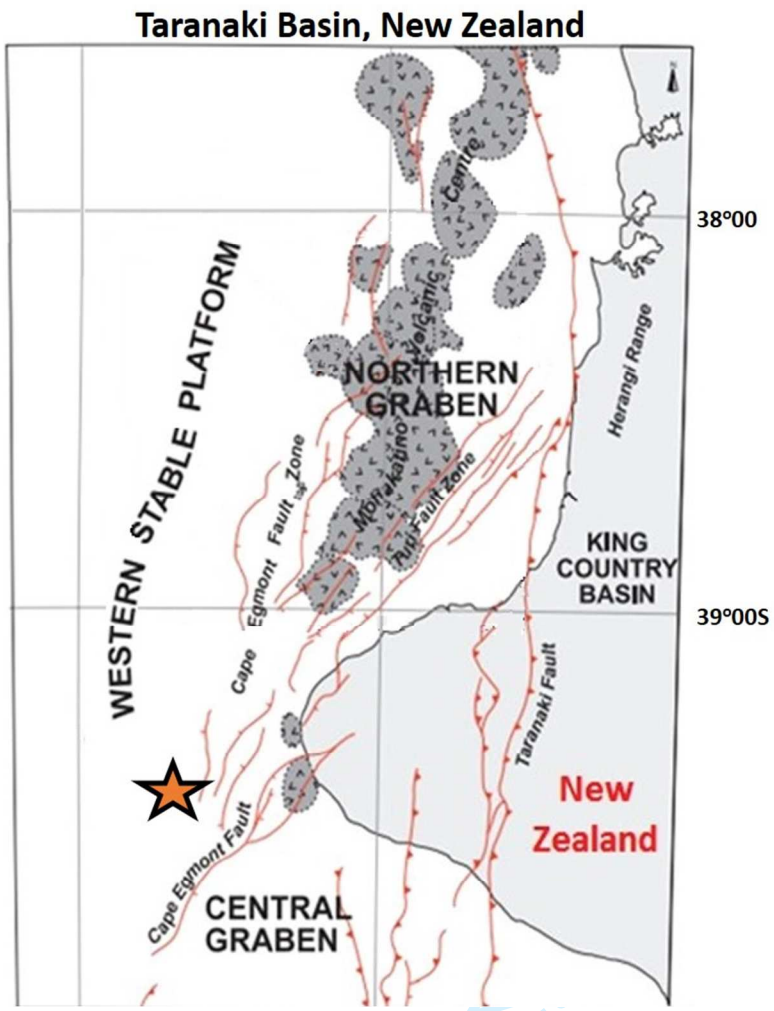
Taranaki Basin, New Zealand
38°00
39°00S
WESTERN STABLE PLATFORM
NORTHERN GRABEN
CENTRAL GRABEN
KING COUNTRY BASIN
Herangi Range
Cape Egmont Fault Zone
Mohakatino Volcanic Centre
Turi Fault Zone
Taranaki Fault
Cape Egmont Fault
New Zealand

Figure 4.

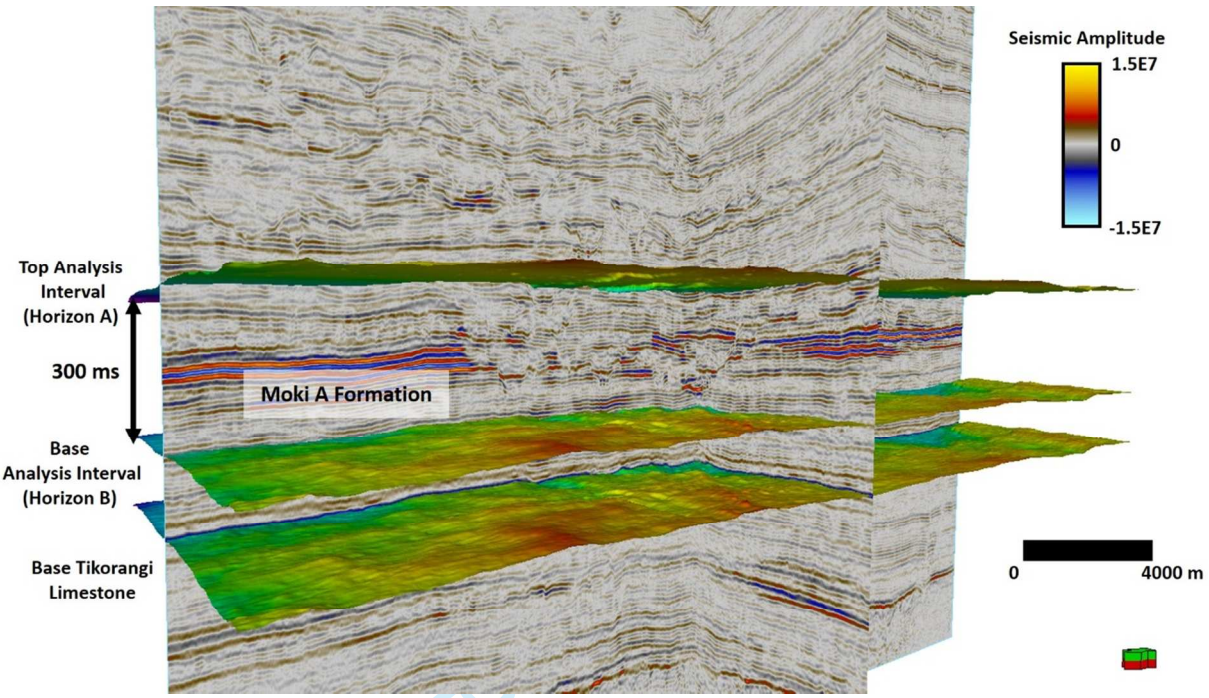

Figure 5.

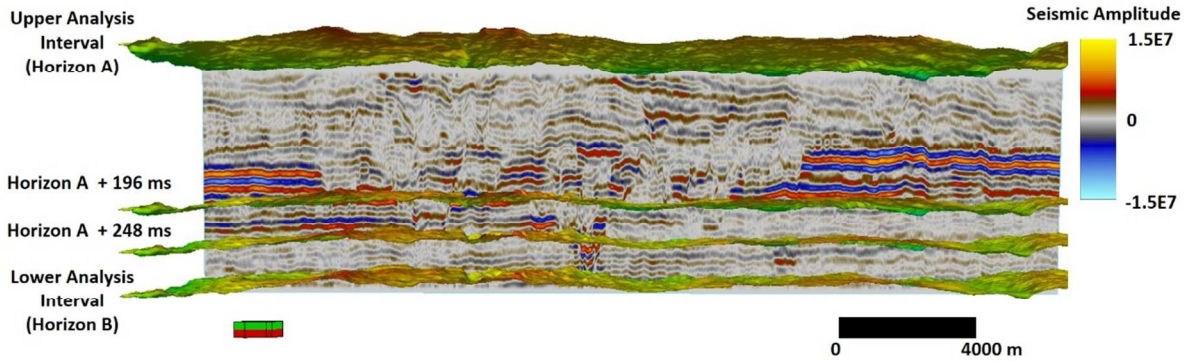

Figure 6.

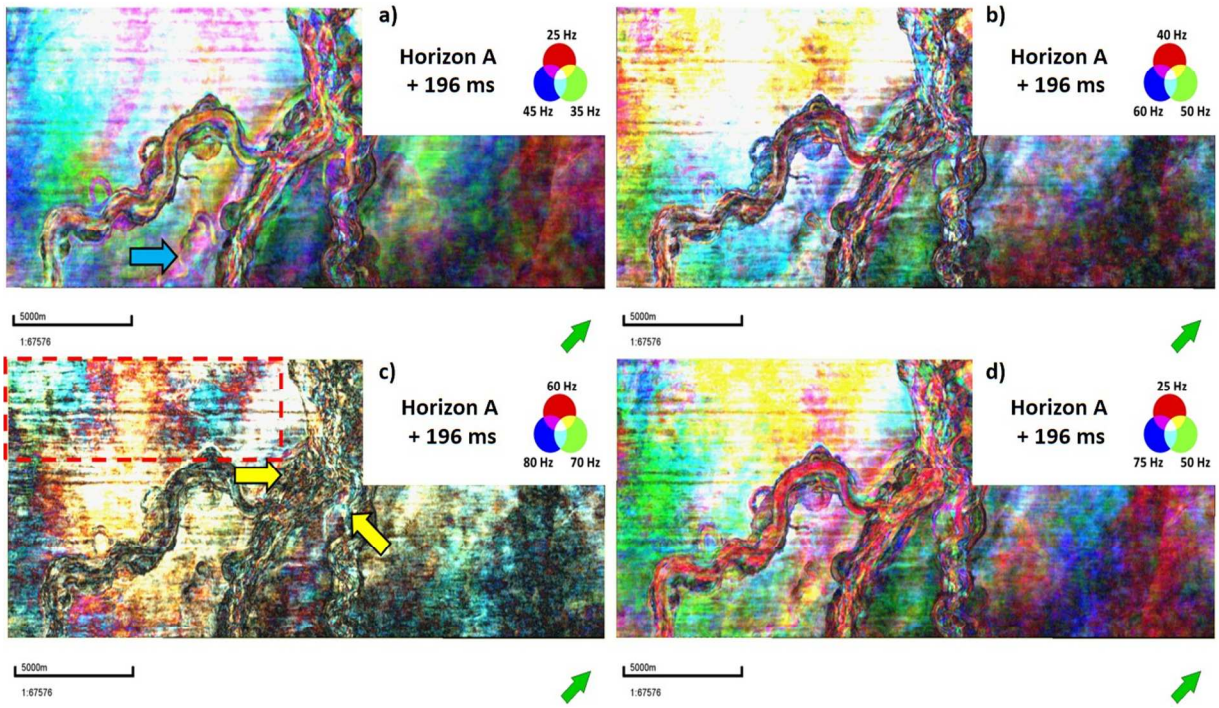

Figure 7.

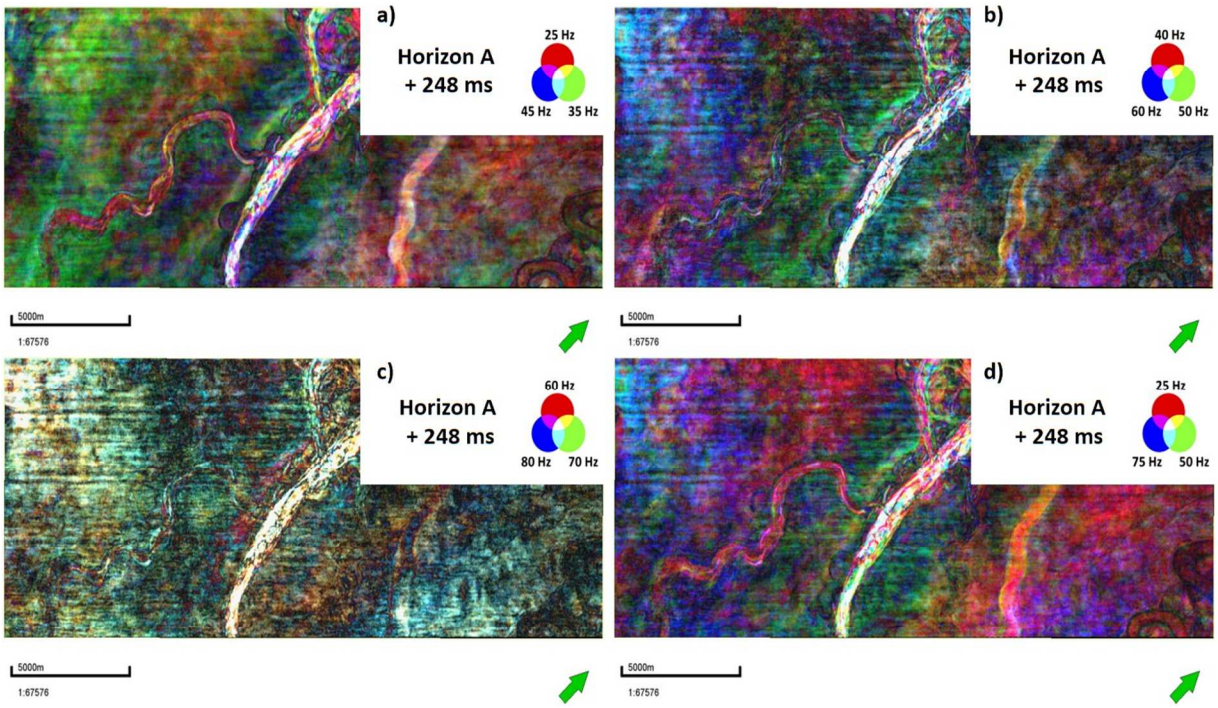

Figure 8.

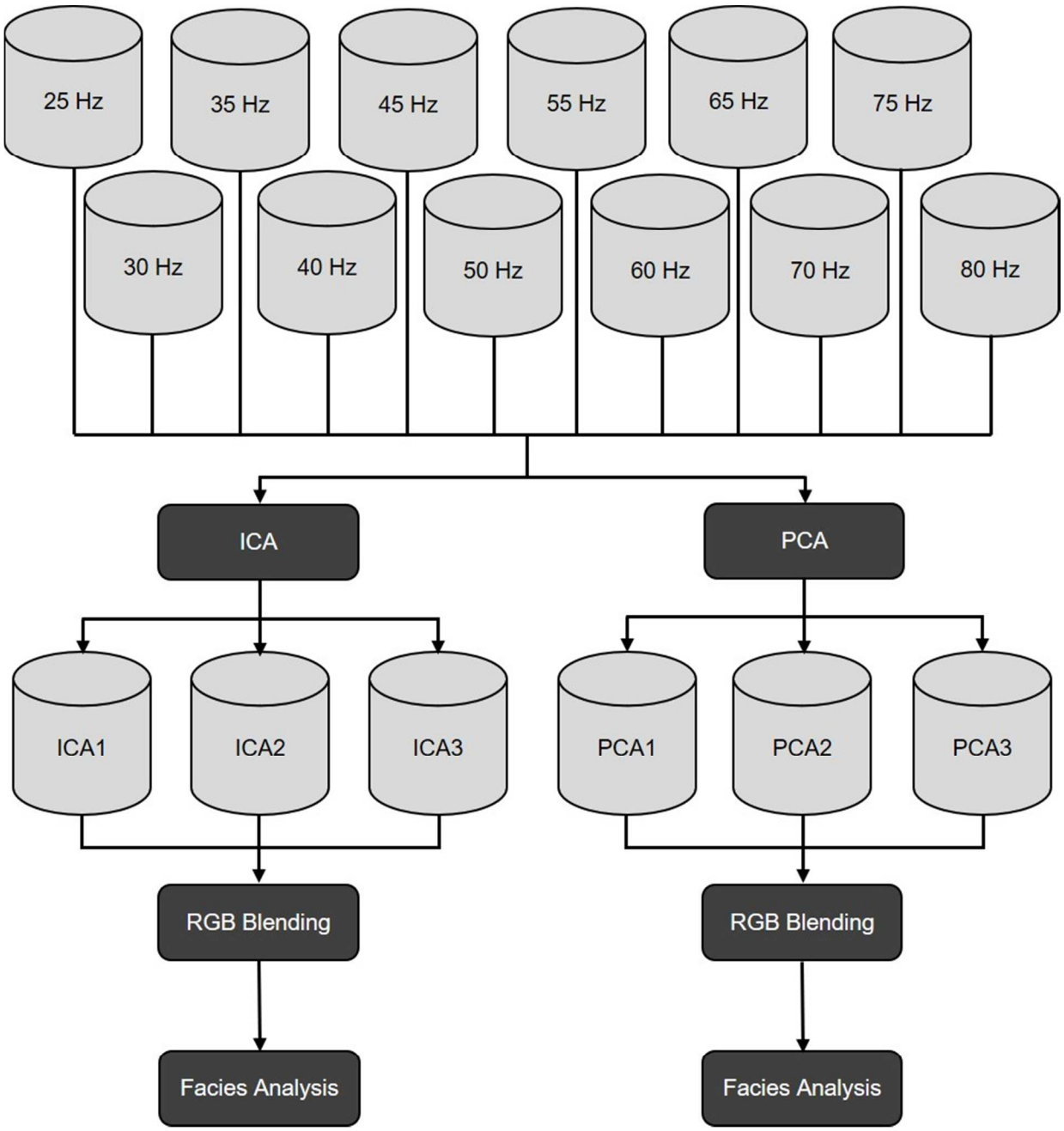
25 Hz
35 Hz
45 Hz
55 Hz
65 Hz
75 Hz
30 Hz
40 Hz
50 Hz
60 Hz
70 Hz
80 Hz
ICA
PCA
ICA1
ICA2
ICA3
PCA1
PCA2
PCA3
RGB Blending
RGB Blending
Facies Analysis
Facies Analysis

Figure 9.

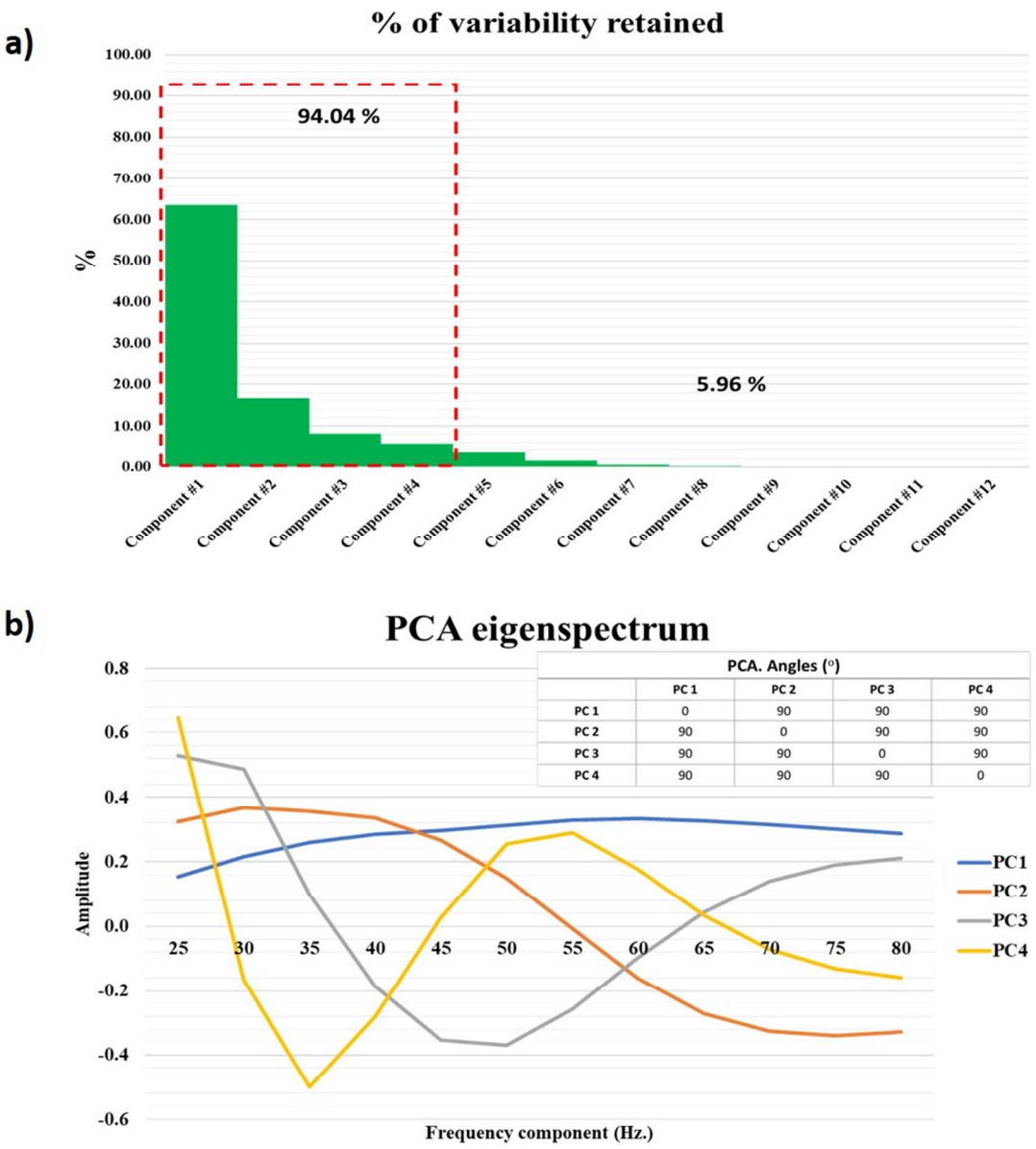
a)
% of variability retained
100.00
90.00
80.00
70.00
60.00
50.00
40.00
30.00
20.00
10.00
0.00
%
94.04 %
5.96 %
Component #1
Component #2
Component #3
Component #4
Component #5
Component #6
Component #7
Component #8
Component #9
Component #10
Component #11
Component #12
b)
PCA eigenspectrum
PCA. Angles (°)
PC 1 PC 2 PC 3 PC 4
PC 1 0 90 90 90
PC 2 90 0 90 90
PC 3 90 90 0 90
PC 4 90 90 90 0
0.8
0.6
0.4
0.2
0.0
-0.2
-0.4
-0.6
Amplitude
25 30 35 40 45 50 55 60 65 70 75 80
Frequency component (Hz.)
PC1
PC2
PC3
PC4

Figure 10.

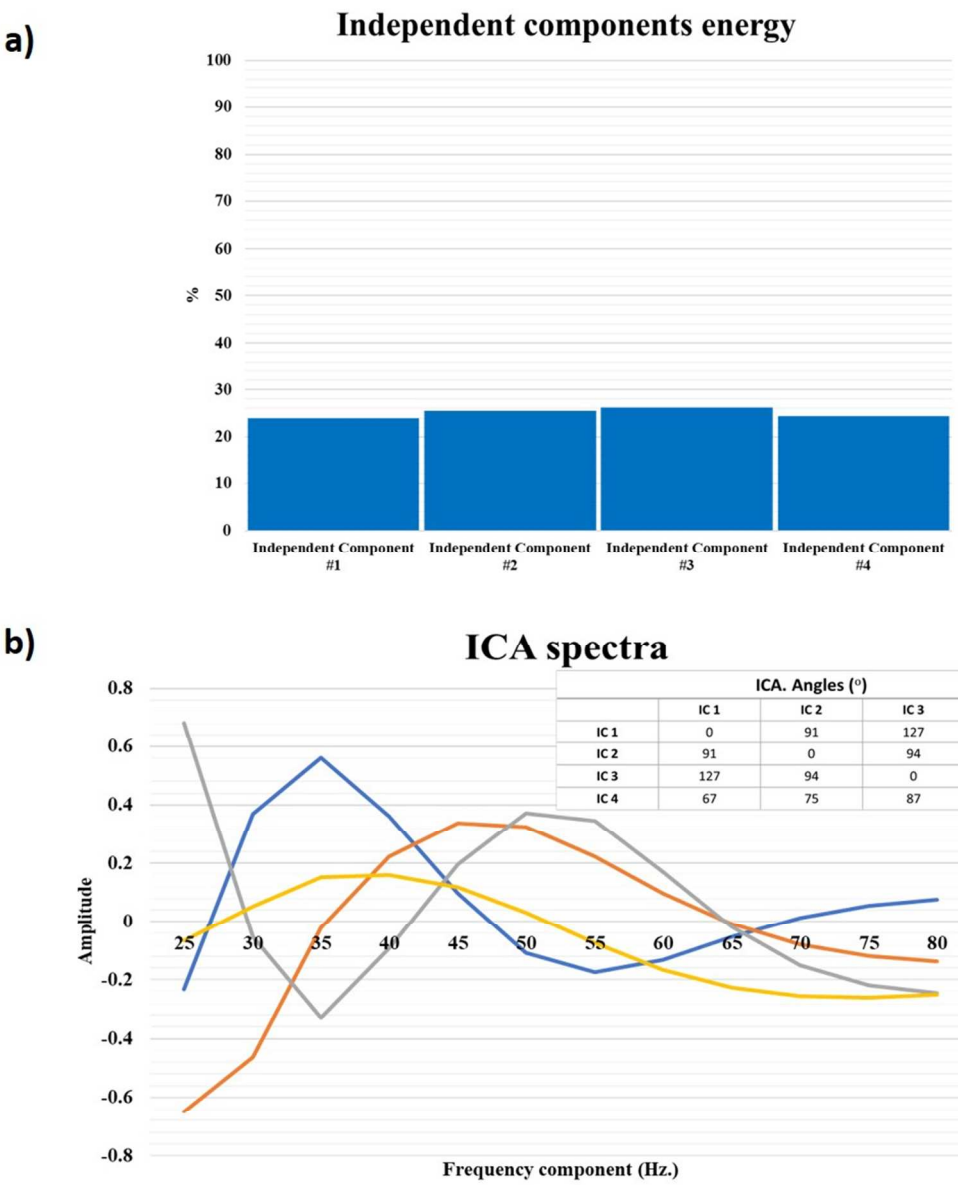
a)
Independent components energy
100
90
80
70
60
50
40
30
20
10
0
%
Independent Component #1
Independent Component #2
Independent Component #3
Independent Component #4
b)
ICA spectra
ICA. Angles (°)
IC 1 IC 2 IC 3 IC 4
IC 1 0 91 127 67
IC 2 91 0 94 75
IC 3 127 94 0 87
IC 4 67 75 87 0
0.8
0.6
0.4
0.2
0
-0.2
-0.4
-0.6
-0.8
Amplitude
25 30 35 40 45 50 55 60 65 70 75 80
Frequency component (Hz.)
IC1
IC2
IC3
IC4

Figure 11.

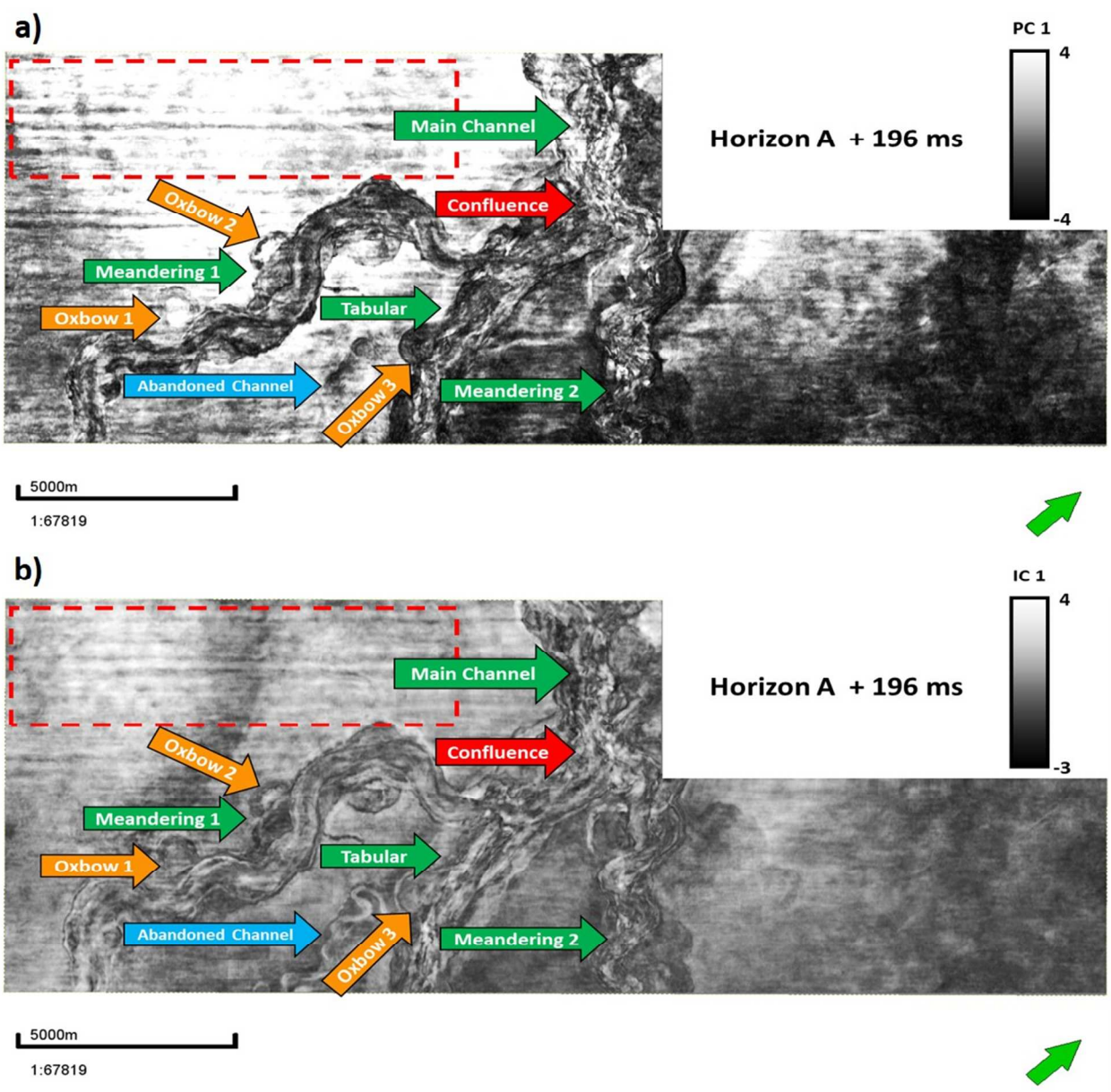
a)
PC 1
4
-4
Horizon A + 196 ms
Main Channel
Confluence
Oxbow 2
Meandering 1
Oxbow 1
Tabular
Abandoned Channel
Oxbow 3
Meandering 2
5000m
1:67819
b)
IC 1
4
-3
Horizon A + 196 ms
Main Channel
Confluence
Oxbow 2
Meandering 1
Oxbow 1
Tabular
Abandoned Channel
Oxbow 3
Meandering 2
5000m
1:67819

Figure 12.

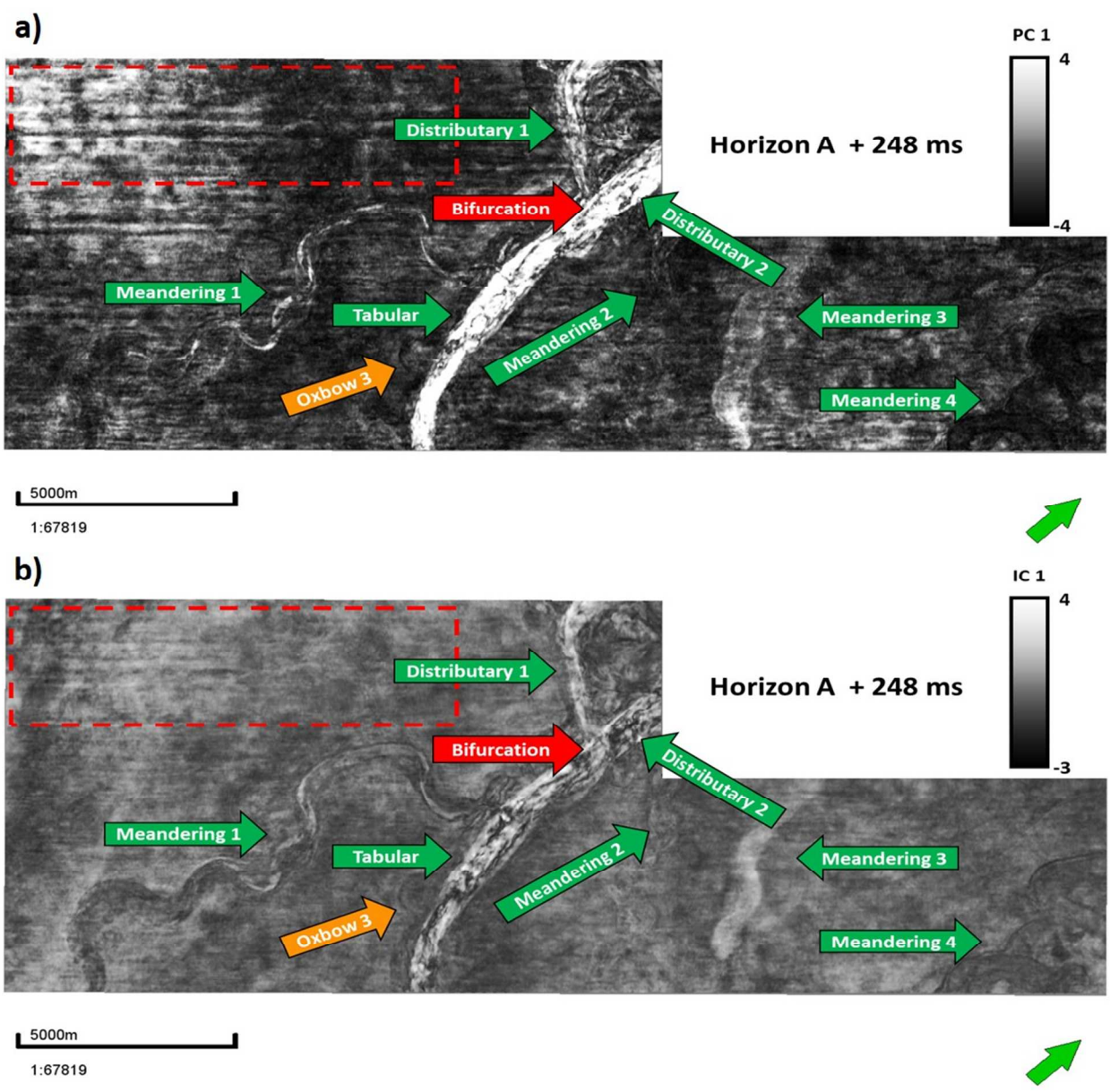
a)
PC 1
4
-4
Horizon A + 248 ms
Distributary 1
Bifurcation
Distributary 2
Meandering 1
Tabular
Meandering 2
Meandering 3
Oxbow 3
Meandering 4
5000m
1:67819
b)
IC 1
4
-3
Horizon A + 248 ms
Distributary 1
Bifurcation
Distributary 2
Meandering 1
Tabular
Meandering 2
Meandering 3
Oxbow 3
Meandering 4
5000m
1:67819

Figure 13.

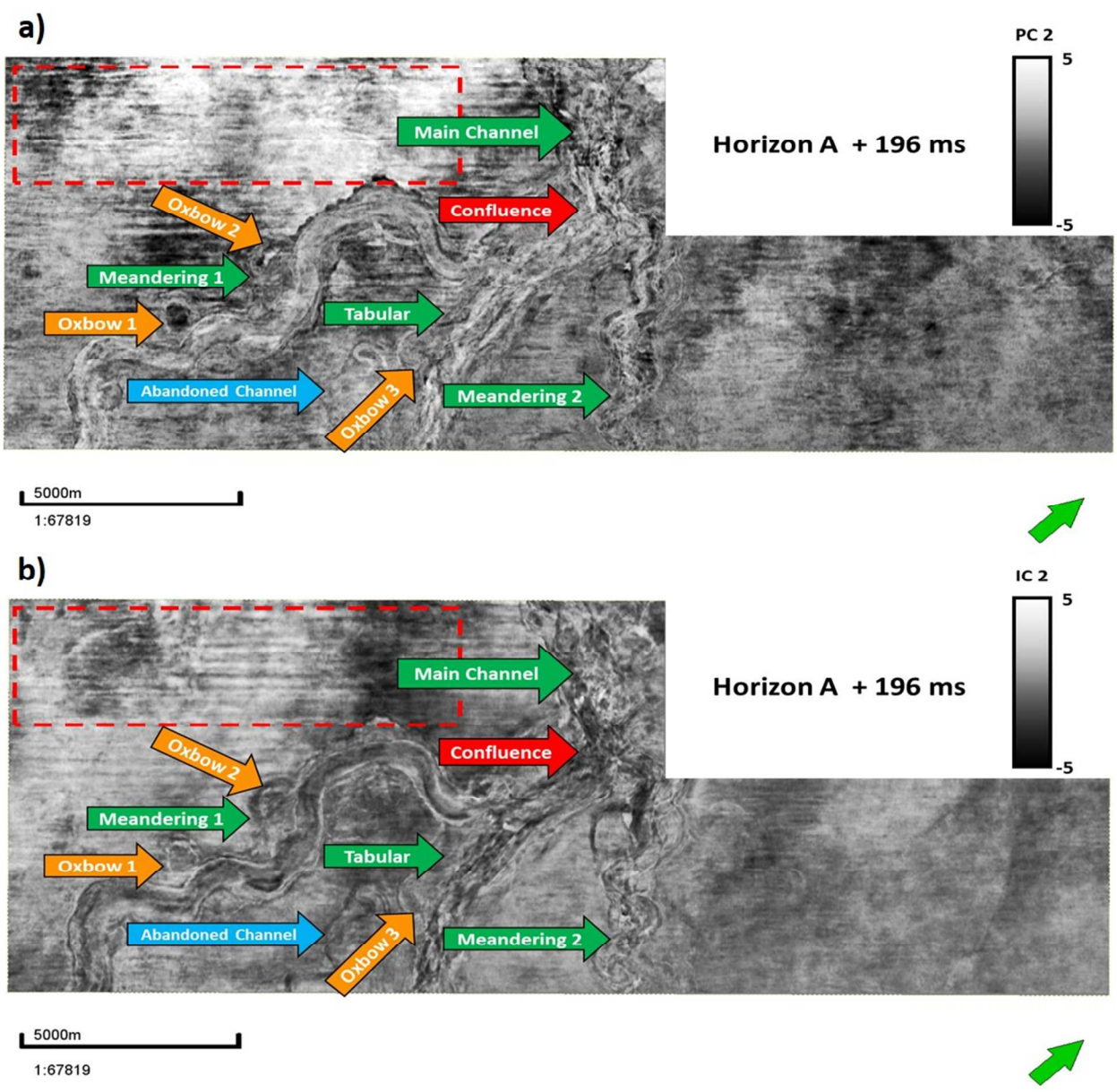
a)
PC 2
5
-5
Horizon A + 196 ms
Main Channel
Confluence
Oxbow 2
Meandering 1
Oxbow 1
Tabular
Abandoned Channel
Oxbow 3
Meandering 2
5000m
1:67819
b)
IC 2
5
-5
Horizon A + 196 ms
Main Channel
Confluence
Oxbow 2
Meandering 1
Oxbow 1
Tabular
Abandoned Channel
Oxbow 3
Meandering 2
5000m
1:67819

Figure 14.

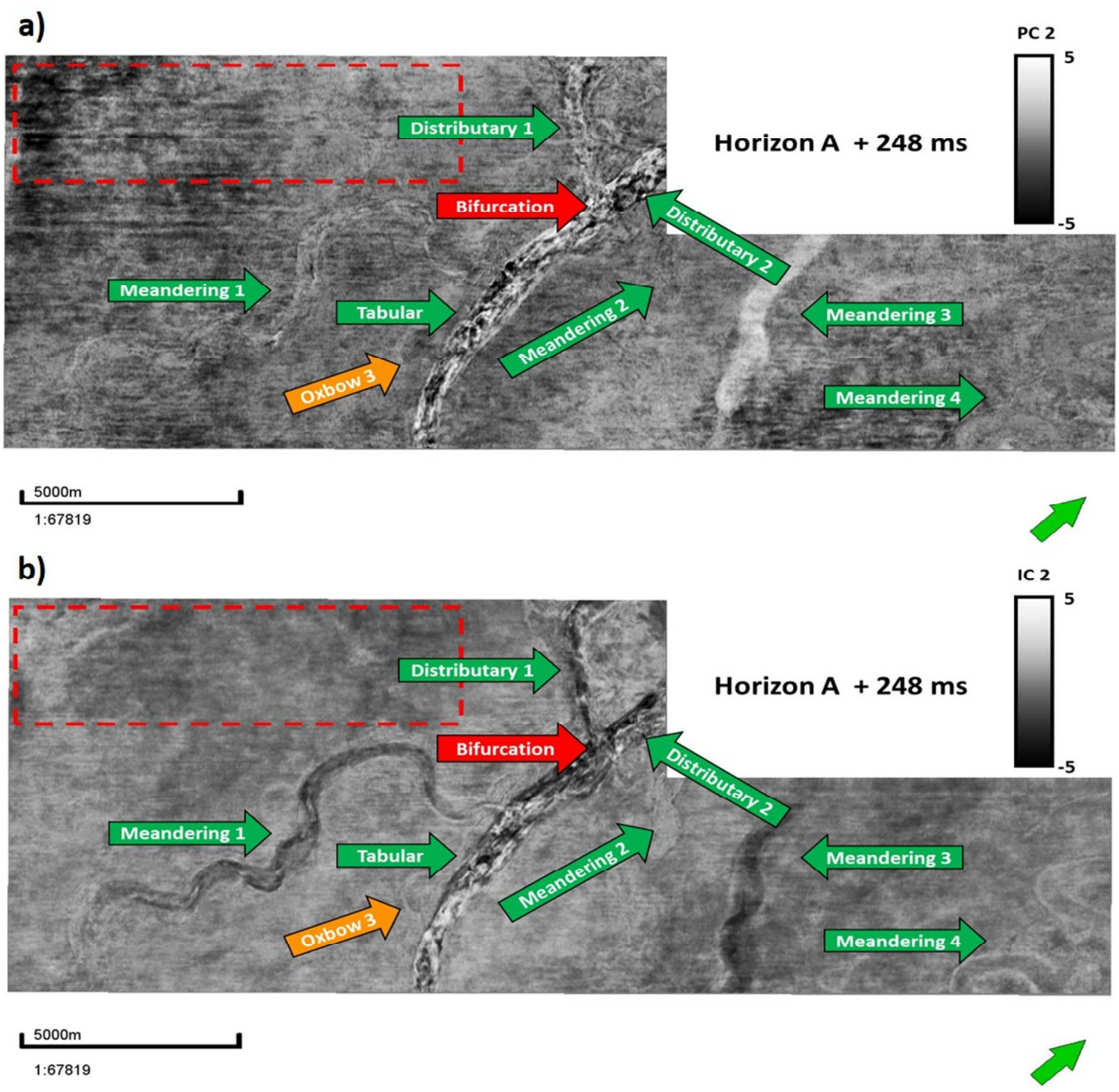
a)
PC 2
5
-5
Horizon A + 248 ms
Distributary 1
Bifurcation
Distributary 2
Meandering 1
Tabular
Meandering 2
Meandering 3
Oxbow 3
Meandering 4
5000m
1:67819
b)
IC 2
5
-5
Horizon A + 248 ms
Distributary 1
Bifurcation
Distributary 2
Meandering 1
Tabular
Meandering 2
Meandering 3
Oxbow 3
Meandering 4
5000m
1:67819

Figure 15.

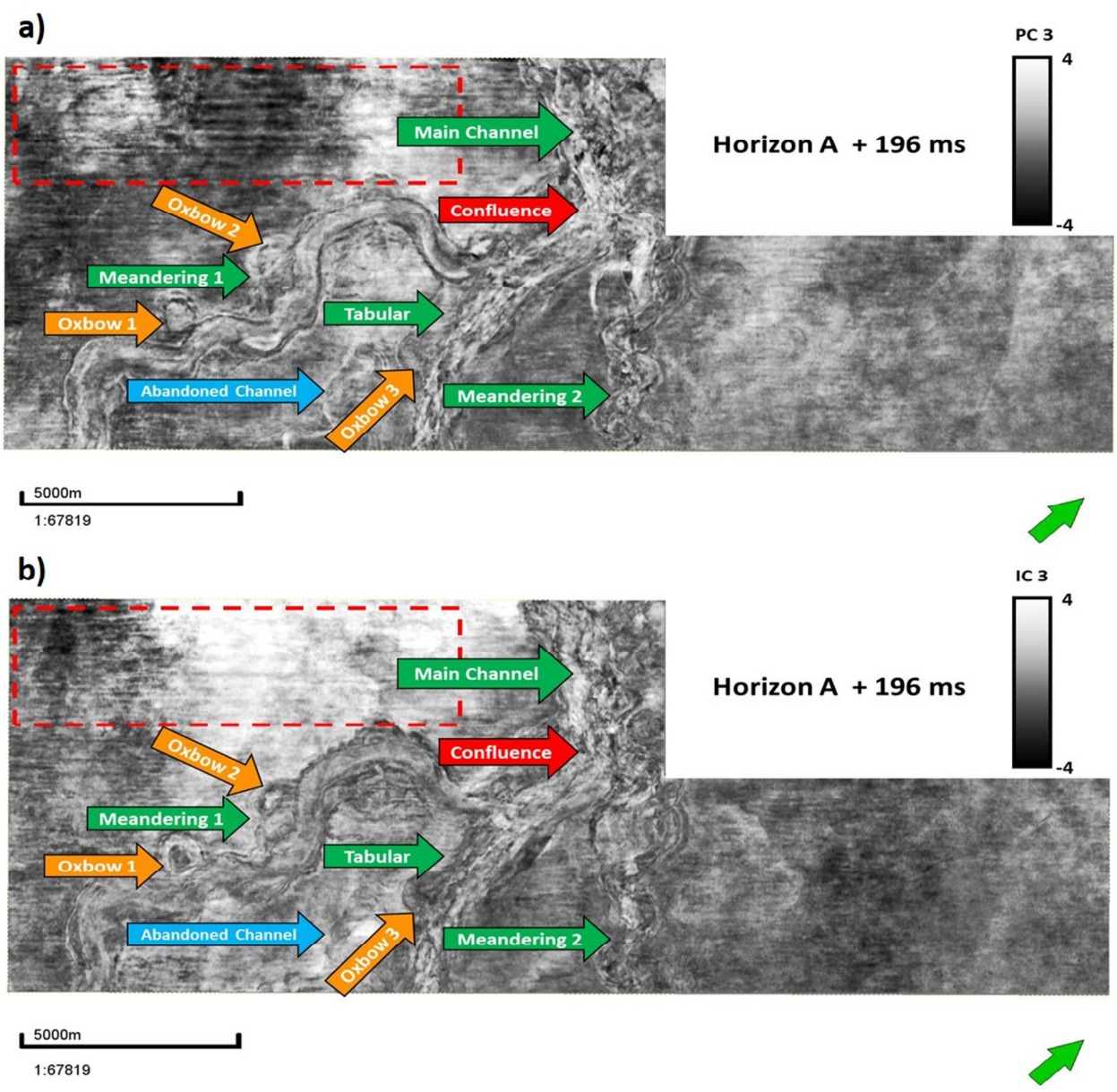
a)
PC 3
4
-4
Horizon A + 196 ms
Main Channel
Confluence
Oxbow 2
Meandering 1
Oxbow 1
Tabular
Abandoned Channel
Oxbow 3
Meandering 2
5000m
1:67819
b)
IC 3
4
-4
Horizon A + 196 ms
Main Channel
Confluence
Oxbow 2
Meandering 1
Oxbow 1
Tabular
Abandoned Channel
Oxbow 3
Meandering 2
5000m
1:67819

Figure 16.

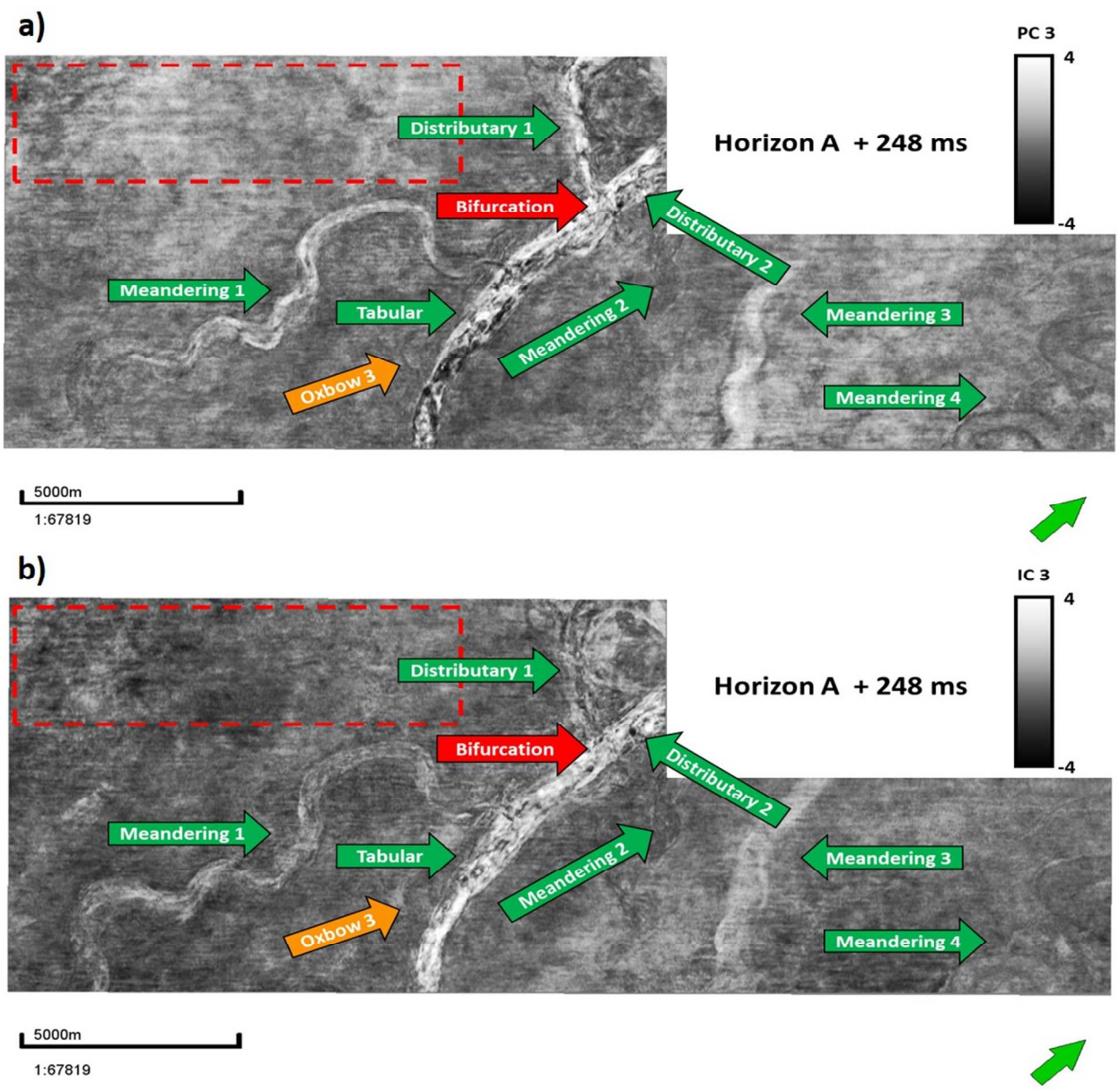
a)
PC 3
4
-4
Horizon A + 248 ms
Distributary 1
Bifurcation
Distributary 2
Meandering 1
Tabular
Meandering 2
Meandering 3
Oxbow 3
Meandering 4
5000m
1:67819
b)
IC 3
4
-4
Horizon A + 248 ms
Distributary 1
Bifurcation
Distributary 2
Meandering 1
Tabular
Meandering 2
Meandering 3
Oxbow 3
Meandering 4
5000m
1:67819

Figure 17.

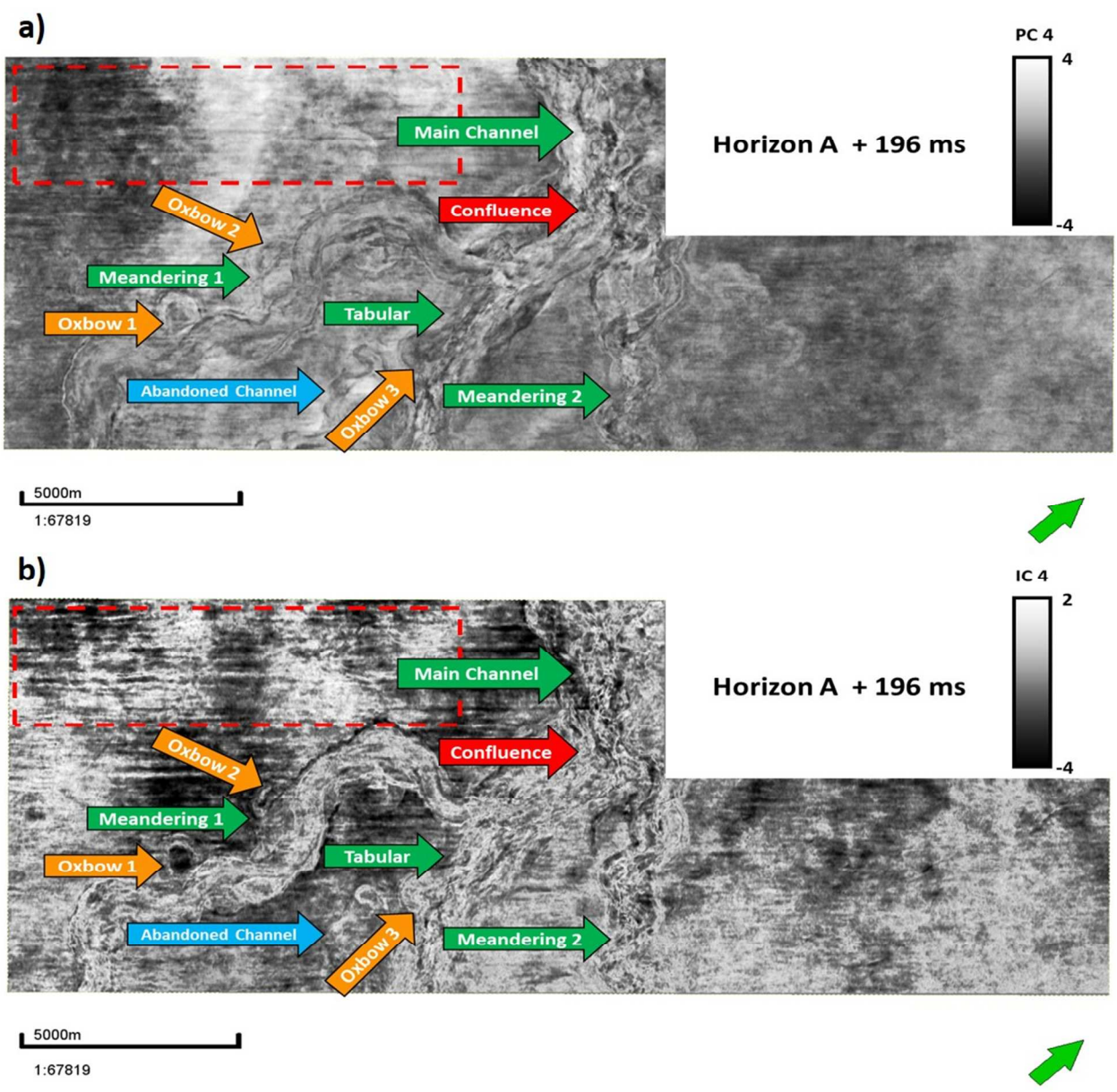
a)
PC 4
4
-4
Horizon A + 196 ms
Main Channel
Confluence
Oxbow 2
Meandering 1
Oxbow 1
Tabular
Abandoned Channel
Oxbow 3
Meandering 2
5000m
1:67819
b)
IC 4
2
-4
Horizon A + 196 ms
Main Channel
Confluence
Oxbow 2
Meandering 1
Oxbow 1
Tabular
Abandoned Channel
Oxbow 3
Meandering 2
5000m
1:67819

Figure 18.

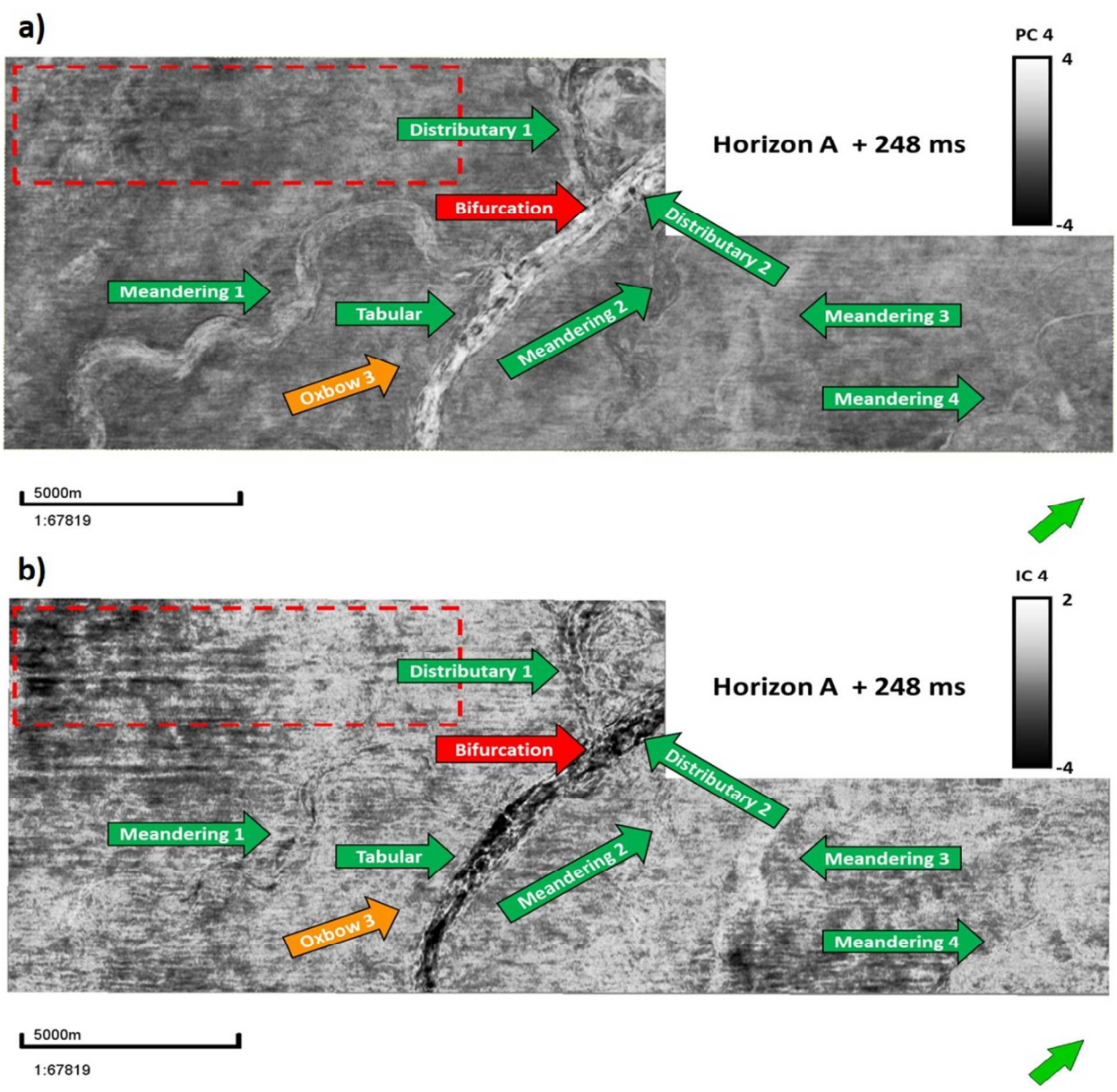
a)
PC 4
4
-4
Horizon A + 248 ms
Distributary 1
Bifurcation
Distributary 2
Meandering 1
Tabular
Meandering 2
Meandering 3
Oxbow 3
Meandering 4
5000m
1:67819
b)
IC 4
2
-4
Horizon A + 248 ms
Distributary 1
Bifurcation
Distributary 2
Meandering 1
Tabular
Meandering 2
Meandering 3
Oxbow 3
Meandering 4
5000m
1:67819

Figure 19.

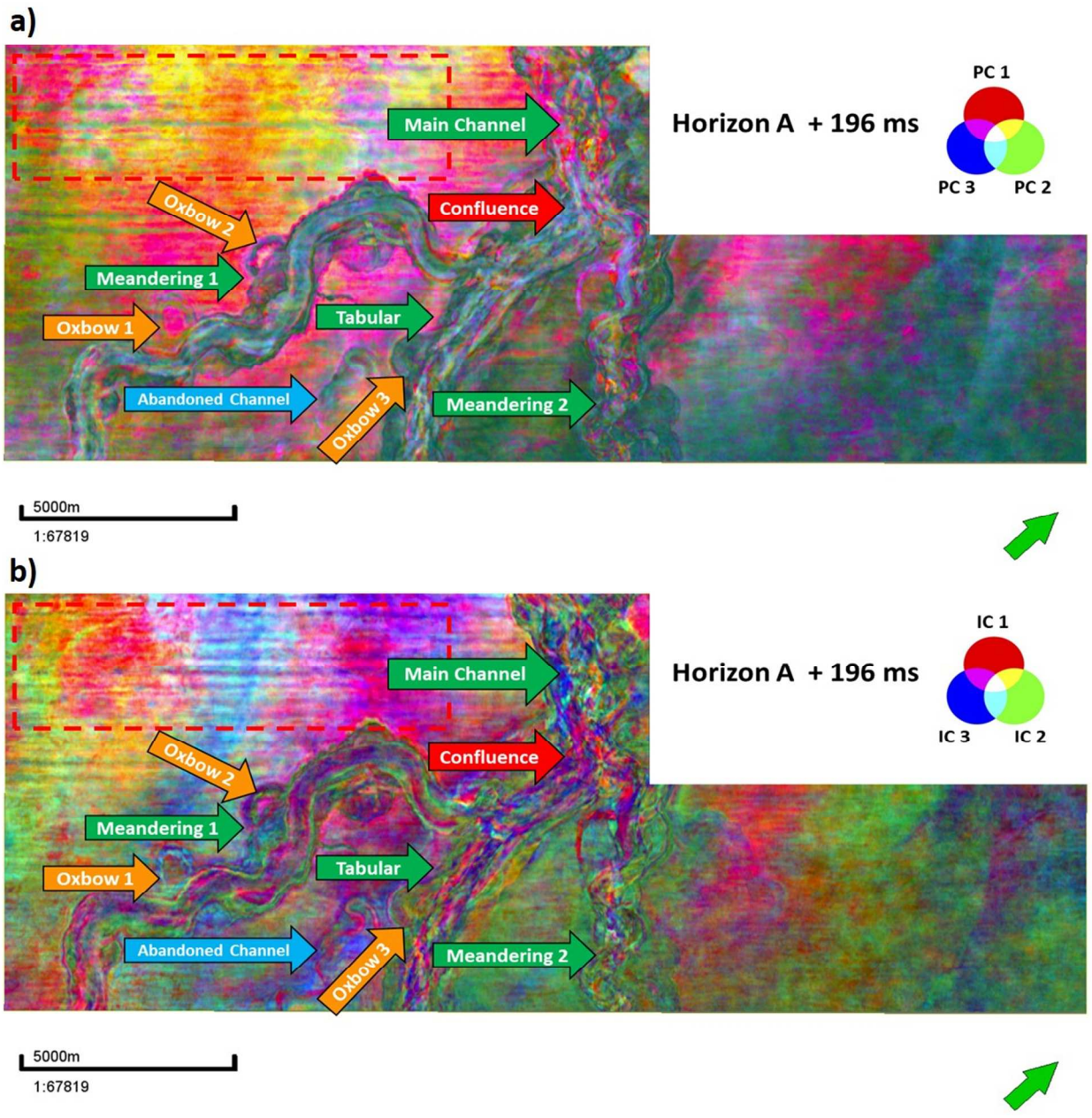
a)
Main Channel
Confluence
Oxbow 2
Meandering 1
Oxbow 1
Tabular
Abandoned Channel
Oxbow 3
Meandering 2
Horizon A + 196 ms
PC 1
PC 3
PC 2
5000m
1:67819
b)
Main Channel
Confluence
Oxbow 2
Meandering 1
Oxbow 1
Tabular
Abandoned Channel
Oxbow 3
Meandering 2
Horizon A + 196 ms
IC 1
IC 3
IC 2
5000m
1:67819

Figure 20.

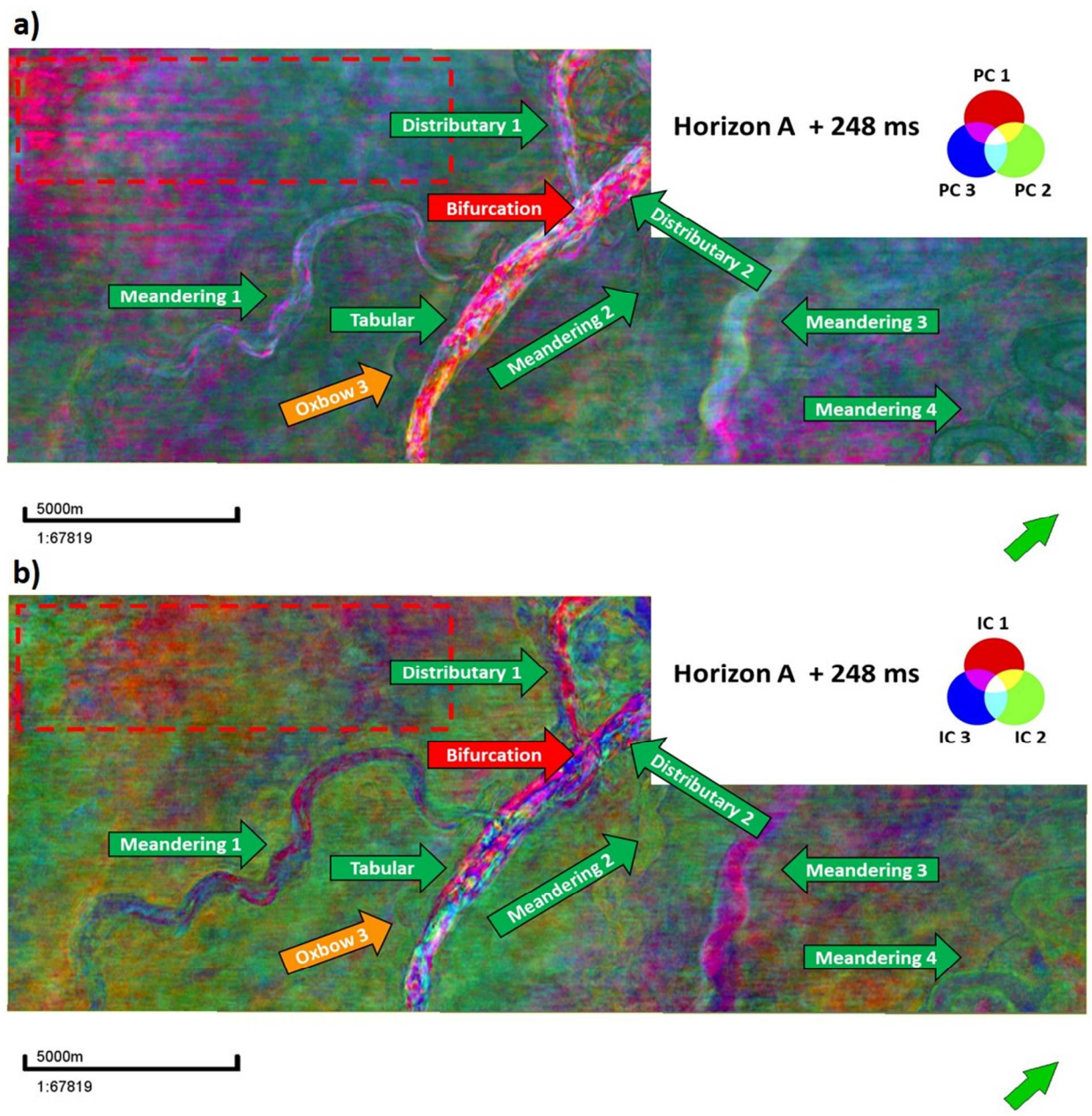
a)
Distributary 1
Horizon A + 248 ms
PC 1
PC 3
PC 2
Bifurcation
Distributary 2
Meandering 1
Tabular
Meandering 2
Meandering 3
Oxbow 3
Meandering 4
5000m
1:67819
b)
Distributary 1
Horizon A + 248 ms
IC 1
IC 3
IC 2
Bifurcation
Distributary 2
Meandering 1
Tabular
Meandering 2
Meandering 3
Oxbow 3
Meandering 4
5000m
1:67819

Figure 21.

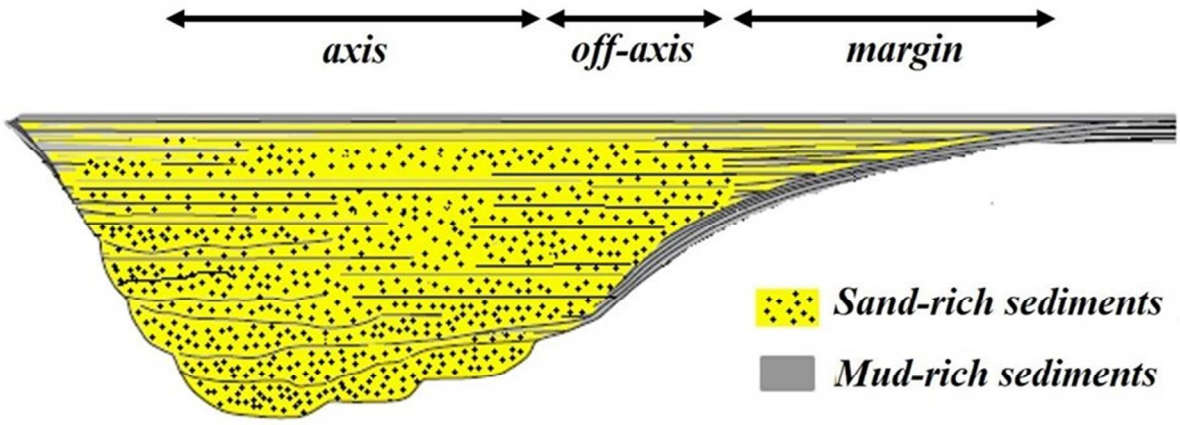

Figure 22.

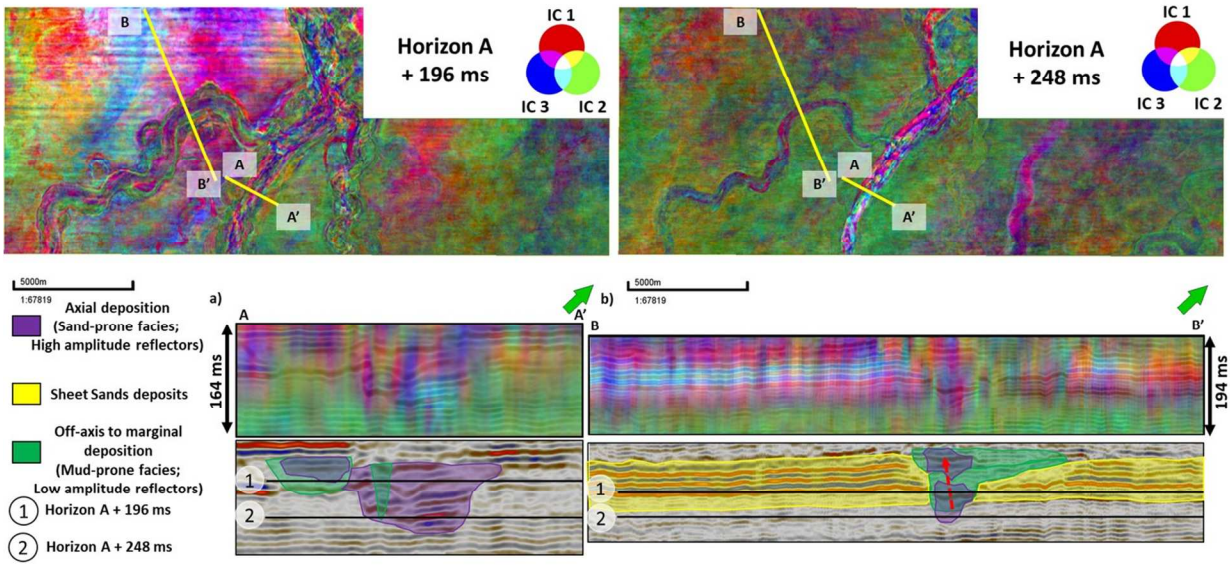

Figure 23.

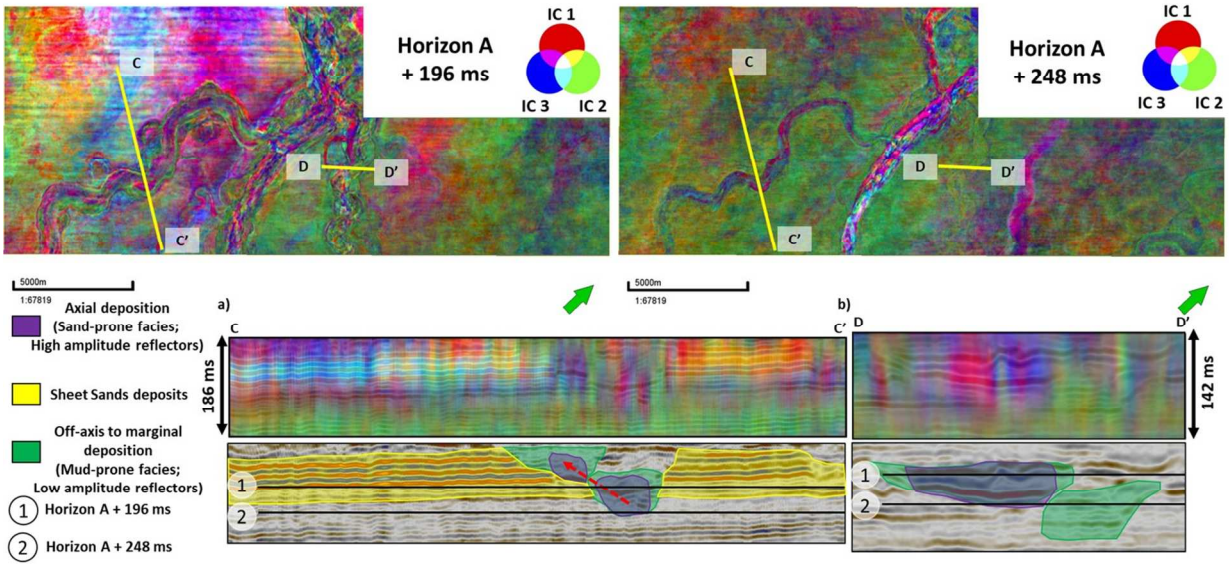

Figure 24.

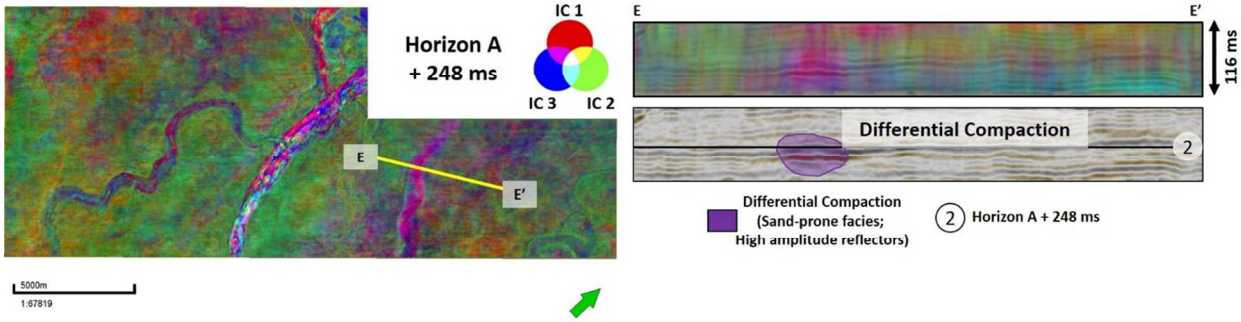

Figure 25.

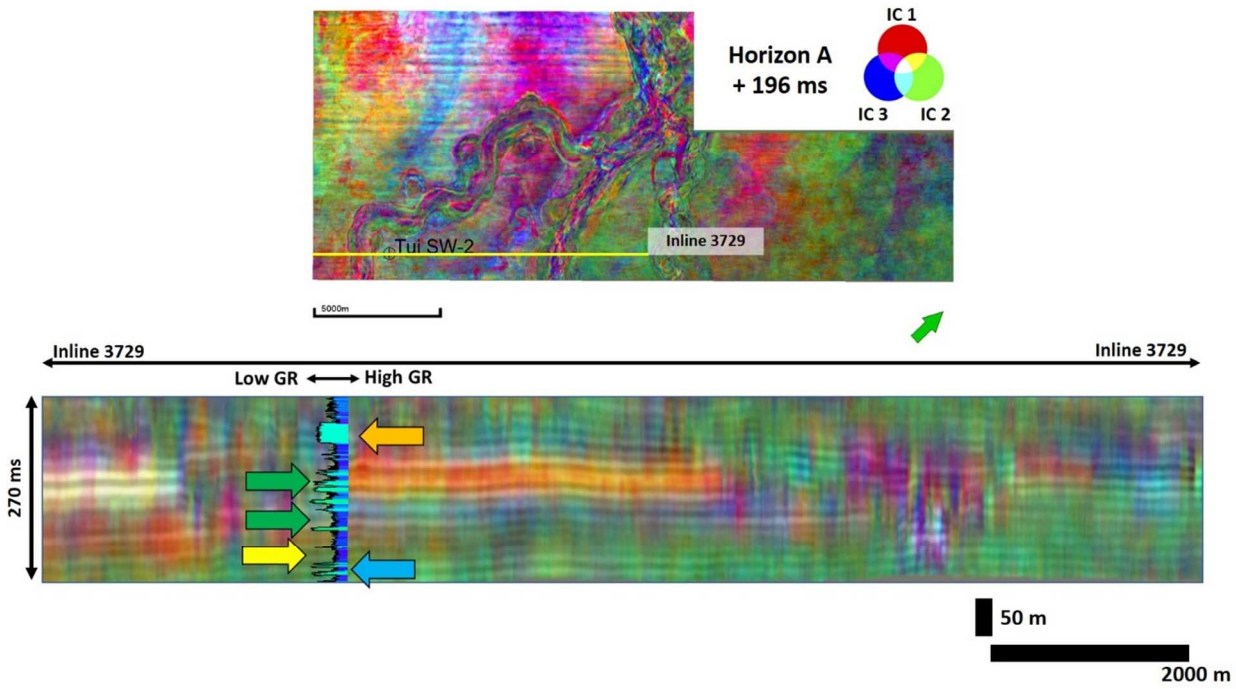

Figure 26.